iScience

CellPress
OPEN ACCESS

Article

Whitening of brown adipose tissue inhibits osteogenic differentiation via secretion of S100A8/A9

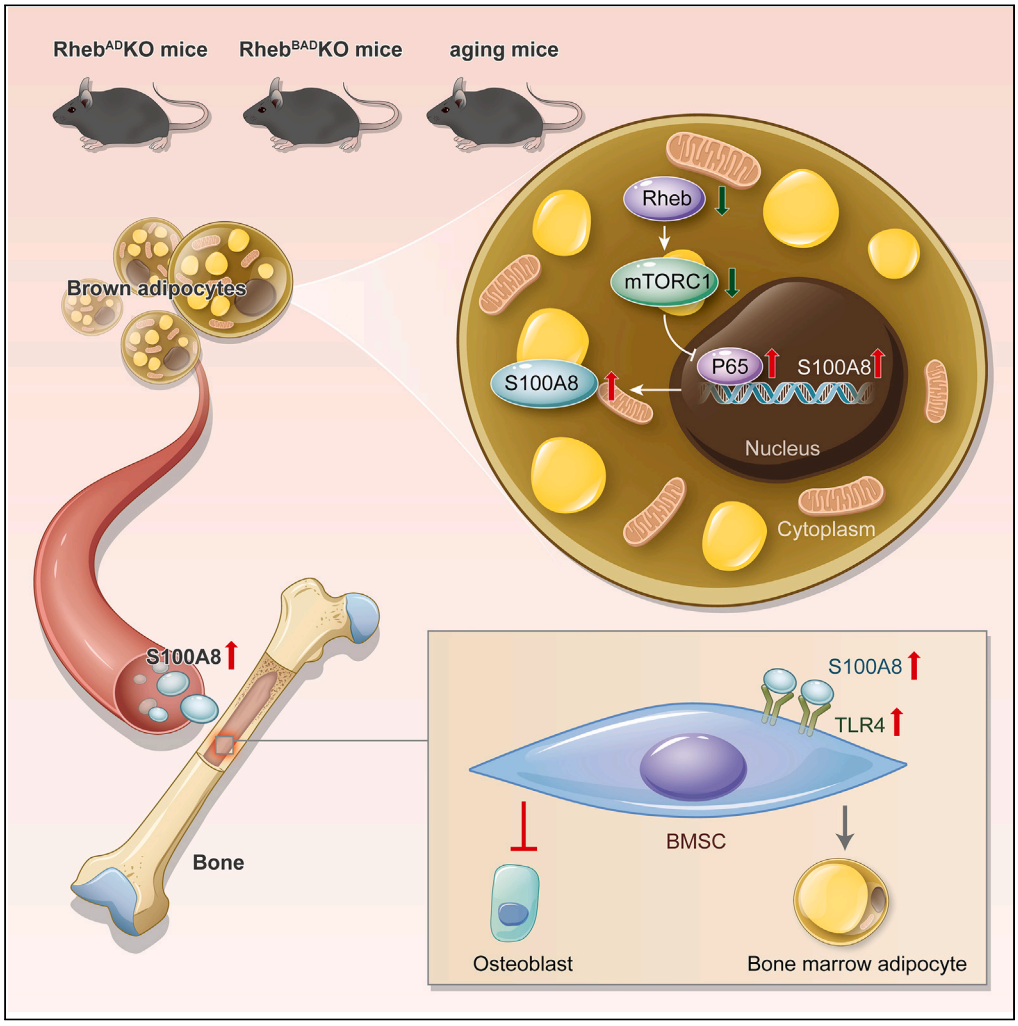

Ting Wang, Chaoran Zhao, Jiahuan Zhang, ..., Anling Liu, Xiaochun Bai, Zhipeng Zou

aliu@smu.edu.cn (A.L.)
baixc15@smu.edu.cn (X.B.)
zzp@smu.edu.cn (Z.Z.)

Highlights

Loss of Rheb induces BAT malfunction and endocrine secretion of S100A8/A9

BAT-derived S100A8/A9 inhibits bone formation, inducing osteoporosis

Neutralizing S100A8/A9 restores bone formation impaired by BAT malfunction

S100A8/A9 directly inhibits osteogenesis of BMSCs by targeting their TLR4

Wang et al., iScience 27, 108857
February 16, 2024
https://doi.org/10.1016/j.isci.2024.108857

iScience

CellPress
OPEN ACCESS

Article

Whitening of brown adipose tissue inhibits osteogenic differentiation via secretion of S100A8/A9

Ting Wang,[1,6] Chaoran Zhao,[1,6] Jiahuan Zhang,[2,6] Shengfa Li,[3,6] Youming Zhang,[1] Yan Gong,[1] Yingyue Zhou,[1] Lei Yan,[1] Sheng Zhang,[1] Zhongmin Zhang,[4] Hongling Hu,[5] Anling Liu,[1,*] Xiaochun Bai,[1,*] and Zhipeng Zou[1,7,*]

SUMMARY

The mechanism by which brown adipose tissue (BAT) regulates bone metabolism is unclear. Here, we reveal that BAT secretes S100A8/A9, a previously unidentified BAT adipokine (batokine), to impair bone formation. Brown adipocytes-specific knockout of *Rheb* (*Rheb*^{BAD} KO), the upstream activator of mTOR, causes BAT malfunction to inhibit osteogenesis. Rheb depletion induces NF-κB dependent S100A8/A9 secretion from brown adipocytes, but not from macrophages. In wild-type mice, age-related Rheb downregulation in BAT is associated with enhanced S100A8/A9 secretion. Either batokines from *Rheb*^{BAD} KO mice, or recombinant S100A8/A9, inhibits osteoblast differentiation of mesenchymal stem cells *in vitro* by targeting toll-like receptor 4 on their surfaces. Conversely, S100A8/A9 neutralization not only rescues the osteogenesis repressed in the *Rheb*^{BAD} KO mice, but also alleviates age-related osteoporosis in wild-type mice. Collectively, our data revealed an unexpected BAT-bone crosstalk driven by Rheb-S100A8/A9, uncovering S100A8/A9 as a promising target for the treatment, and potentially, prevention of osteoporosis.

INTRODUCTION

Brown adipose tissue (BAT) is composed primarily of brown adipocytes (BADs). BAT differs from white adipose tissue (WAT) in that it functions to generate heat by uncoupling mitochondrial respiration from ATP synthesis via uncoupling protein 1 (Ucp1).[1] BAT activation in healthy subjects dramatically improves whole-body glucose and lipid homeostasis, as well as insulin sensitivity.[2–4] Conversely, the whitening (a state in which BAT loses its heat-generating function and gains the features of WAT) and loss of BAT in obesity and aging promotes metabolic disorders and related diseases.[5] These data demonstrate important systemic metabolic functions of BAT beyond heat production. Thus, brown adipokines (so-called "batokines") and their functional role in remote regulation of other organs, either in physiological or pathophysiological conditions, have attracted considerable interest.[6] For instance, BAT secretes FGF21 to protect the heart, induce the browning of WAT, and improve β-cell function,[6,7] myostatin to inhibit skeletal muscle growth,[8] and CXCL14 to coordinate M2 macrophages with BAT activation.[9,10] BAT is potentially associated with bone homeostasis. It has been revealed that BAT volume is positively correlated with the amount of bone in children and adolescents.[11] and with femoral cross-sectional area independent of age.[12] Elderly people exhibit reduced BAT activity,[13] as well as reduced bone mass.[14] In patients with anorexia nervosa, significant bone loss is concomitant with marked reductions in BAT volume and activity.[15–17] On the contrary, FGF21, a metabolic hormone released by liver and thermogenically activated BAT, is associated with increased bone resorption and reduced bone mass in people living with HIV.[18] Despite these indirect evidences, the endocrine role of BAT in bone metabolism, the contributing adipokines, and the underlying mechanism remain largely unclear.

Mechanistic target of rapamycin complex 1(mTORC1) is a central signaling hub controlling biological processes including protein synthesis, autophagy, and lipid metabolism.[19] The GTP-bound form of a small G-protein, RAS homologue enriched in brain (Rheb), binds directly to mTOR and triggers maximum activation of mTORC1.[19] Thus, Rheb loss renders hypoactivation of mTORC1. mTORC1 promotes adipogenesis and enhances lipogenesis *in vitro* and *in vivo*.[20,21] However, the role of mTORC1 in BAT homeostasis is uncertain due to the lack of animal models with BAT-specific inactivation of mTORC1. Additionally, the role of mTORC1 in the endocrine secretion of BAT remains elusive.

[1]Guangdong Provincial Key Laboratory of Bone and Joint Degeneration Diseases, Department of Cell Biology, School of Basic Medical Sciences, Southern Medical University, Guangzhou 510515, China
[2]Laboratory Medicine, Guangdong Provincial People's Hospital (Guangdong Academy of Medical Sciences), Southern Medical University, Guangzhou, China
[3]Clinical Research Center, Zhujiang Hospital, Southern Medical University, Guangzhou, China
[4]Division of Spine Surgery, Department of Orthopadics, Nanfang Hospital, Southern Medical University, Guangzhou, China
[5]Department of Trauma and Joint Surgery, Shunde Hospital, Southern Medical University, Foshan, China
[6]These authors contributed equally
[7]Lead contact
*Correspondence: aliu@smu.edu.cn (A.L.), baixc15@smu.edu.cn (X.B.), zzp@smu.edu.cn (Z.Z.)
https://doi.org/10.1016/j.isci.2024.108857

In the present study, we serendipitously found that loss of Rheb in BAT compromises bone formation, in addition to the BAT dysfunction. We revealed that brown adipocytes secrete S100A8/A9, an inflammatory alarmin thought to be preferentially secreted by immune-activated myeloid cells, to suppress osteogenesis of bone marrow mesenchymal stem cells (BMSCs).

RESULTS

Deletion of Rheb drives BAT whitening

To unravel the potential role of Rheb in maintenance of BAT homeostasis, as well as the role of BAT in bone metabolism, we generated mice with BAD-specific *Rheb* deletion (*Rheb*^{BAD} KO) control of the *Ucp1* promoter (illustrated in Figure S1A)[22] to confirm its effect on BAT function. As expected, Rheb was successfully depleted in interscapular BAT (Figure S1B). UCP1 protein was downregulated in inguinal WAT (iWAT), and epididymal WAT (eWAT) of *Rheb*^{BAD} KO mice, in comparison with the control mice, although basal UCP1 expression in eWAT of control mice was nearly invisible (Figure S1C). To verify the specific expression of *Ucp1-Cre* in BADs, the *Ucp1-Cre* mice were crossed with *ROSA*$^{mT/mG}$ mice. As anticipated, *Ucp1-Cre* was expressed specifically in BADs, but not in the stromal cells (including macrophages) in interscapular BAT, nor in the WAT (Figure S1D). Consistently, no prominent Rheb depletion was observed in the major organs (Figure S1E). Body weight of the control and *Rheb*^{BAD} KO mice were comparable (Figure S1F). A recent study demonstrated non-specific expression of Ucp1 in ventromedial hypothalamus (VMH), one of the critical regions responsible for the regulation of energy homeostasis.[23] Thus, we further examined Rheb expression in VMH of the control and *Rheb*^{BAD} KO mice but found no significant difference between these two types of mice (Figure S1G). The interscapular BAT of *Rheb*^{BAD} KO mice showed conspicuous "whitening" and reduced size, as observed by gross examination (Figure 1A), HE staining (Figure 1B), IHC (Figure 1C), as well as western blotting (WB) analysis (Figure 1D). The BAT of these mice also showed increased expression of Nrip1 (Figure 1E). Similarly, the inguinal WAT of *Rheb*^{BAD} KO mice also showed certain degree of "whitening" (Figure S2A). Several circulating metabolic markers were also analyzed. No significant difference in serum triglyceride level was observed between the control and *Rheb*^{BAD} KO mice. Free fatty acids (FFA) and glycerol were markedly higher in *Rheb*^{BAD} KO mice (Figure S2B), which is consistent with elevated expression of genes critical for lipolysis, including adipose triglyceride lipase (ATGL) and hormone-sensitive lipase (HSL), in these mice (Figure S2C). Additionally, the phosphorylation of HSL protein was also enhanced in the KO mice (Figure S2D). The observed increase in BAT lipolysis may result from Rheb loss and consequent inactivation of mTOR, which suppresses lipolysis but promotes lipogenesis and fat storage.[24,25]

To further examine the effect of BAD-specific Rheb loss on thermogenesis, the control and KO mice were subjected to cold acclimation at 4°C for 7 days. Then, we analyzed the expression of several thermogenic genes in BAT, including those involved in creatine metabolism, which was documented to induce compensatory thermogenesis in the absence of UCP1.[26] Among these genes, while Cidea mRNA expression was significantly reduced (Figure S2E), Ckmt1 and GAMT was significantly increased in the BAT of the KO mice (Figure S2F), which may compensate the cold adaptation of KO mice. UCP-1 expression level in the BAT of wild-type C57BL6/J mice increased continuously from 30°C to 4°C (Figure S2G), confirming that the temperature environment we used was suitable. Rheb expression decreased moderately at both 30°C and 4°C (Figure S2G), suggesting that its expression may be independent of the documented elevation of mTOR activity responsive to cold exposure.[27] The oxygen consumption and energy expenditure of the *Rheb*^{BAD} KO mice was significantly increased, in comparison with the control mice (Figure S2H), without prominent change in respiratory exchange rate and food intake (Figure S2I). These seemingly contradictory results suggest that reduced UCP1-dependent thermogenesis in BAT may be complicated by increased lipolysis, compensatory induction of creatine metabolism, and potential increased energy consumption of other organs.

Glucose tolerance test and insulin tolerance test were performed to analyze the effect of Rheb loss in BAD on global glucose metabolism. Glucose tolerance was significantly reduced in the *Rheb*^{BAD} KO mice (Figure S2J), reflecting that glucose clearance by BAT is impaired by Rheb loss. However, these KO mice did not exhibit significant change in global insulin sensitivity (Figure S2K), suggesting that insulin-responsive glucose uptake may not be affected in other tissues, including skeletal muscle, which accounts for far more total body glucose use than BAT.[28] Collectively, these results strongly suggested that Rheb is essential for the maintenance of BAT phenotype and function.

Adipocytic *Rheb* gene knockout mice (under the control of *Fabp4/aP2* promoter, named thereafter *Rheb*^{AD} KO) were also generated (illustrated in Figure S3A) to confirm the functional role of Rheb in BAT, although this *Cre* line was show to target other cell types including macrophages, nerve cells, and cardiac epithelia.[29–31] As expected, Rheb was successfully depleted in interscapular BAT, as well as in inguinal and epididymal WAT (Figure S3B). While the interscapular BAT pads of *Rheb*^{AD} KO mice were significantly lighter and smaller than those of control mice, no marked difference was observed in either inguinal or epididymal WAT between the control and *Rheb*^{AD} KO mice (Figures S3C and S3D). Likewise, no significant differences in either weight or size of major organs (Figure S3E) or in serum leptin, an adipose-derived hormone that circulates in proportion to WAT mass (Figure S3F), were observed between the control and *Rheb*^{AD} KO mice. Interestingly, *Rheb*^{AD} KO mice displayed dramatically augmented adipocyte size (manifested as increased mean size as well as more large adipocytes) predominantly in BAT (Figure S4A), suggesting that BAT activity is markedly decreased in these mice. Indeed, multilocular adipocytes in interscapular BAT in the control mice were replaced by unilocular adipocytes in *Rheb*^{AD} KO mice (Figure S4A). Consistently, *Rheb*^{AD} KO mice demonstrated a dramatic reduction in expression of BAT markers, such as Ucp1, PRDM16, and Ppargc1a, in their interscapular BAT, as observed by immunohistochemical (IHC) staining (Figure S4B). Western blotting confirmed UCP1 protein was downregulated in BAT, iWAT, and eWAT of these KO mice, in comparison with the control mice, although basal UCP1 expression in eWAT of control mice cannot be constantly detected (Figure S4C). After a 7-day cold adaptation, *Rheb*^{AD} KO mice exhibited compensatory expression changes of thermogenic genes similar to *Rheb*^{BAD} KO mice (Figures S4D and S4E). Besides, the inguinal WAT of *Rheb*^{AD} KO mice, which contains a certain number of beige

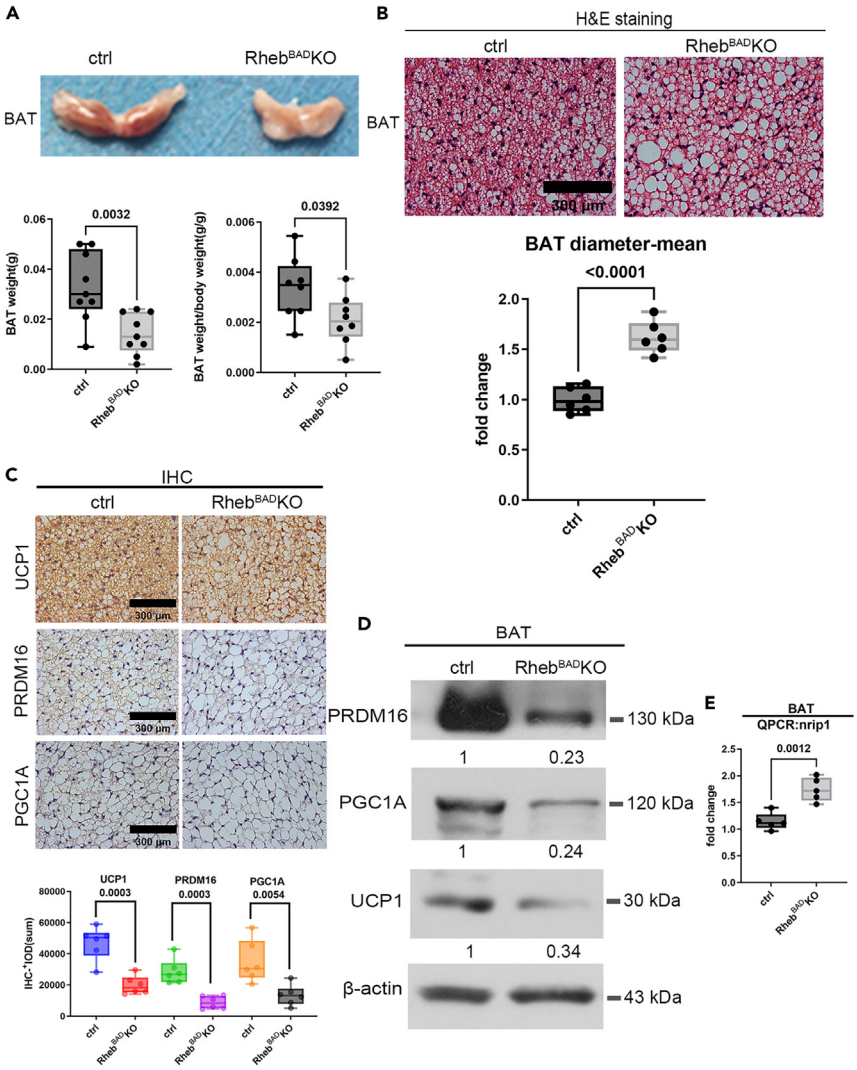

Figure 1. Deletion of Rheb drives BAT whitening

(A) Gross examination (upper panel) and weight statistics (lower panel) of the BAT of the control and *Rheb*$^{FL/FL}$; *Ucp1-Cre* (*Rheb*^{BAD} KO) mice.

(B) H&E or (C) immunohistochemical (IHC) staining of the BAT sections from the control and *Rheb*^{BAD} KO mice for the indicated markers.

(D) WB analysis of the BAT tissue from these mice for the indicated proteins.

(E) RT-qPCR assay for Nrip expression in the BAT of the control and Rheb^{BAD} KO mice. Data are shown as box-and-whisker plots (with median and interquartile ranges) from max to min, with all data points shown. Analyses were performed as two-tailed unpaired t-test.

adipocytes, also showed signs of reduced "browning", as evident by weakened expression of PRDM16 and enhanced expression of Nrip1, a marker of BAT de-differentiation and whitening (Figure S4F).[32]

BAT in C57BL/6J mice shows significant "whitening" due to aging.[33] To further characterize the functional role of Rheb in BAT homeostasis, Rheb protein expression in BAT of wild-type C57BL/6J mice was analyzed. Concomitant with significant "whitening" (Figures S5A and S5B) and reduced expression of key functional proteins of BAT (Figure S5C), interscapular BAT in aged mice (20 months old) showed a marked reduction in Rheb protein expression, when compared with their young counterparts (3 months old) (Figure S5C). This suggests that loss of Rheb is associated with age-dependent BAT "whitening" and dysfunction.

Rheb ablation in BAT resulted in reduced trabecular bone formation, but increased bone marrow fat in mice

Cancellous bone of distal femur/proximal tibia C57BL/6 mice exhibit significant age-related bone loss, regardless of their sex. Thus, this strain serves as a useful model for the study of age-related osteoporosis (AOP).[34,35] To focus on the estrogen-independent role of BAT in AOP, we selected male *Rheb*^{AD} KO and *Rheb*^{BAD} KO mice to evaluate the causal relationship of BAT dysfunction with AOP. Remarkably, *Rheb*^{AD} KO and *Rheb*^{BAD} KO mice showed markedly reduced trabecular bone mass (BV/TV), bone mineral density (BMD), trabecular thickness (Tb.Th),

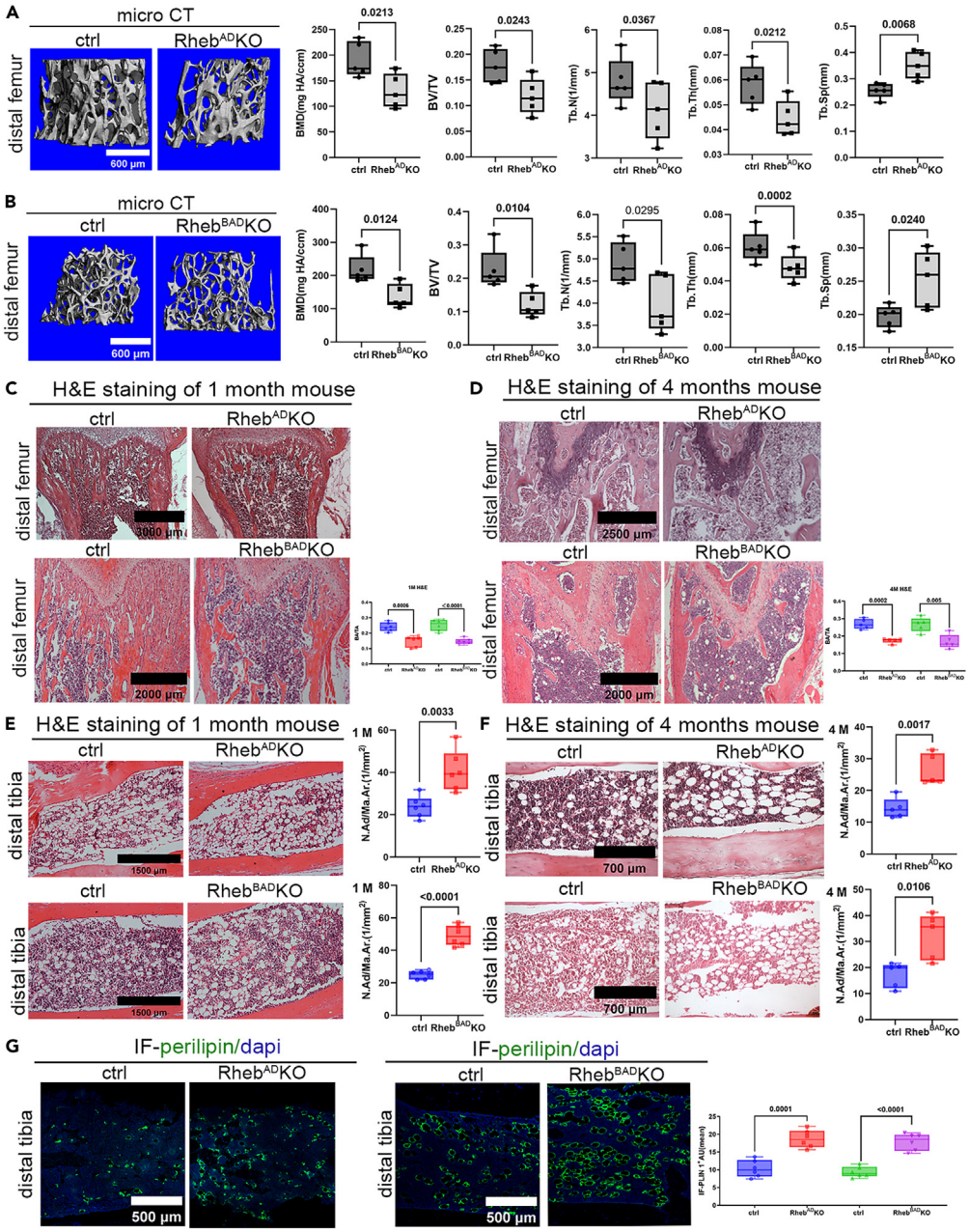

Figure 2. Rheb ablation in BAT resulted in reduced bone mass, but increased bone marrow fat in mice

Three-dimensional microCT reconstruction (left panel) and histomorphometric analysis (right panel) of distal femora and proximal tibiae from the control and *Rheb*^{AD} KO mice (A), or the control and *Rheb*^{BAD} KO mice (B), were performed. Hematoxylin–eosin (HE) analysis of distal femora and proximal tibiae from 1-month-old (C) and 4-month-old (D) control and *Rheb*^{AD} KO mice (upper panel), or control and *Rheb*^{BAD} KO mice (lower panel). Marrow fat in the medullary cavity of distal tibiae from the 1-month-old (E) and 4-month-old (F) control and *Rheb*^{AD} KO mice (upper panel), or the control and *Rheb*^{BAD} KO mice (lower panel) was examined by HE staining. Representative images were shown left, while quantitation of the number of marrow adipocytes were shown right.

(G) Marrow fat in the medullary cavity of distal tibiae from the control and *Rheb*^{AD} KO, or from the control and *Rheb*^{BAD} KO mice was examined by IF staining of Perilipin. Data are shown as box-and-whisker plots (with median and interquartile ranges) from max to min, with all data points shown. Analyses of **Figure** 2A-D, 2G were performed as two-tailed unpaired t-test.

and trabeculae numbers (Tb.N), but increased trabecular separation (Tb. Sp) compared to their control littermates at 1 and 4 months of age, as visualized by three-dimensional microCT (Figures 2A and 2B) and HE analysis (Figures 2C and 2D) of distal femora. However, neither *Rheb*^{AD} KO mice nor *Rheb*^{BAD} KO mice showed prominent alteration in cortical bone parameters, in comparison with their control littermates (Figures S6A and S6B), suggesting that their BAT dysfunction mainly affects trabecular bone.

Conversely, the number of adipocytes in the bone marrow, which appear as oval vacuoles by HE staining, was higher in distal tibiae in *Rheb*^{AD} KO mice and *Rheb*^{BAD} KO mice than their control littermates (Figures 2E and 2F). Furthermore, the expression of perilipin, a marker for mature adipocytes, was enhanced in the bone marrow of both types of *Rheb* knockout mice (Figure 2G).

In *Rheb*^{BAD} KO mice, expression of *Ucp1-Cre* was not observed in cells located at the trabeculae or lacunae, nor at the periosteum (Figure S7A). Additionally, Rheb protein expression was similar in these cells of both control and *Rheb*^{AD} KO mice (Figure S7B). These results suggest the osteopenic phenotype observed in *Rheb*^{AD} KO mice and *Rheb*^{BAD} KO mice cannot be attributed to nonspecific knockout of Rheb in preosteoblasts, osteoblasts (OBs), osteocytes, or osteoclasts (OCs).

Rheb ablation in BAT led to reduced osteoblast differentiation *in vivo* and *ex vivo*

Rheb^{AD} KO and *Rheb*^{BAD} KO mice displayed a marked decrease in osteoblast (OB) differentiation, respectively (Figures 3A and 3B). Consistently, these mice also demonstrated significantly lowered expression of both Osx (Figure 3C) and Ocn (Figure 3D). *Rheb*^{BAD} KO mice also showed markedly reduced mineral apposition rate (MAR) in comparison with their control littermates, as quantified by calcein labeling (Figure 3E). However, the number of TRAP-positive OCs was also lower in *Rheb*^{AD} KO and *Rheb*^{BAD} KO mice (Figure 3F). Consistently, both types of KO mice displayed a marked decrease both in serum Procollagen I N-Terminal Propeptide (PINP), a circulating marker for new bone formation, and in Cross Linked C-Telopeptide of Type I Collagen (CTX-I), a serum marker for bone resorption (Figure 3G).[36] The reason remains unknown, but we speculate that it may reflect a decoupled state of bone formation and resorption after BAT dysfunction. Moreover, BMSCs isolated from the femoral marrow cavity of these two types of mice displayed a greatly reduced capacity for OB differentiation (Figure 3H), but significantly enhanced adipocyte differentiation (Figure 3I), without noticeable change in the expression of Rheb itself (Figure 3J). These results collectively suggest that the impaired osteogenesis of these mice may be driven by a reduction in OB lineage commitment of BMSCs.

The transcriptome of BMSCs isolated from *Rheb*^{BAD} KO mice was subsequently analyzed by whole-genome mRNA array. *Rheb* mRNA expression in BMSCs of *Rheb*^{BAD} KO mice was similar to that of the control mice (Figure S8A), suggesting that there was no nonspecific Rheb knockout in these cells. Consistent with decreased OB differentiation capacity, GO analysis of BMSC transcriptome of *Rheb*^{BAD} KO mice demonstrated down-regulation of genes enriched in ossification, OB differentiation, and bone mineralization, including SP7 (Osx), Prrx2, Ibsp, Fgfr2, and Fgfr3 (Figures S8B and S8C).

Brown but not white adipocytes from Rheb-ablated mice suppress osteoblast differentiation from BMSCs

To investigate whether adipokines from BAT of *Rheb*^{AD} KO mice directly suppress OB differentiation from BMSCs, conditioned medium (CM) collected either from interscapular BADs, or from epididymal WADs of *Rheb*^{AD} KO mice cultured *ex vivo*, was transferred to cultures of primary BMSCs (from wild-type C57BL/6J mice). OB or AD differentiation was then analyzed by ALP staining or oil red O staining, respectively. Interestingly, while CM from BAD of *Rheb*^{AD} KO mice markedly suppressed OB, but promoted AD differentiation (Figures 4A and 4B), CM from WAD had little effect on either OB or AD differentiation (Figures 4C and 4D). This inhibitory effect of BAT adipokines on OB or AD differentiation was verified since CM collected from interscapular BADs of *Rheb*^{BAD} KO mice had similar effects (Figures 4E–4H). In contrast, heat-inactivated CM (heated at 95°C for 10 min to denature any proteins) had little effect on OB or AD differentiation of BMSCs (Figures S9A–S9D). These results suggest that adipokines, but not fatty acids, which were reported to suppress OB differentiation *in vitro*,[37] play a major role in this BAD-OB crosstalk. Collectively, these results suggest that adipokines released from malfunctional BAD, but not WAD, suppress OB but enhance AD differentiation.

Loss of *Rheb* in BAT induces transcription and secretion of S100A8/A9

To further identify the individual adipokines secreted by malfunctional BAT to suppress OB differentiation, a whole-genome mRNA array assay of interscapular BAT was performed. Among the significantly upregulated genes (*Rheb*^{AD} KO mice VS control), inflammation-related genes, including leukocyte chemotaxis, myeloid leukocyte migration, and neutrophil chemotaxis, were highly enriched (Figure 5A). Interestingly, BAT from the *Rheb*^{BAD} KO mice showed upregulated genes enriched in highly similar biological processes (Figure 5B), suggesting that the impaired osteogenesis of both the *Rheb*^{AD} KO mice and the *Rheb*^{BAD} KO mice may be caused by similar BAT-derived inflammatory factors.

The heterodimeric protein S100A8 (MRP8)/A9 (MRP14) is a key inflammation alarmin, which acts as both a diagnostic marker and a critical player during various kinds of inflammatory responses.[38] Remarkably, S100A8 (with a 36.5-fold upregulation in the *Rheb*^{AD} KO mice) and S100A9 (with an 8.91-fold upregulation in *Rheb*^{AD} KO mice), were at the convergence point of these processes (Figure 5C). Marked upregulation of S100A8 and S100A9 was also observed in the BAT of *Rheb*^{BAD} KO mice, as shown by a Volcano plot (Figure 5D). Both RT-qPCR (Figure 5E) and WB (Figure 5F) confirmed that the S100A8 and S100A9 level was elevated in BAT tissues from both types of knockout mice. Importantly, S100A8 and S100A9 protein level was also elevated in serum of these two types of mice (Figure 5G). Since S100A9 usually forms a heterodimer with S100A8 and functions to stabilize S100A8 and increase its protein level,[38] we focused on the function of S100A8/A9 heterodimer, instead of the independent function of S100A8 or S100A9.

Remarkably, aged C57BL/6J mice (20 months old), a native mouse model for both age-related BAT "whitening" and bone loss, also showed increased S100A8 protein levels both in interscapular BAT (Figure 5H) and in serum (Figure 5I), in comparison with their younger counterparts (3 months old). Further, CM from BADs of these aged mice showed much higher S100A8 levels than that from their bone marrow (BM), a major source of myeloid cells including neutrophils and macrophages (Figure 5J). These data collectively suggest that BAT-derived S100A8/A9 may be associated with age-related bone loss in mice.

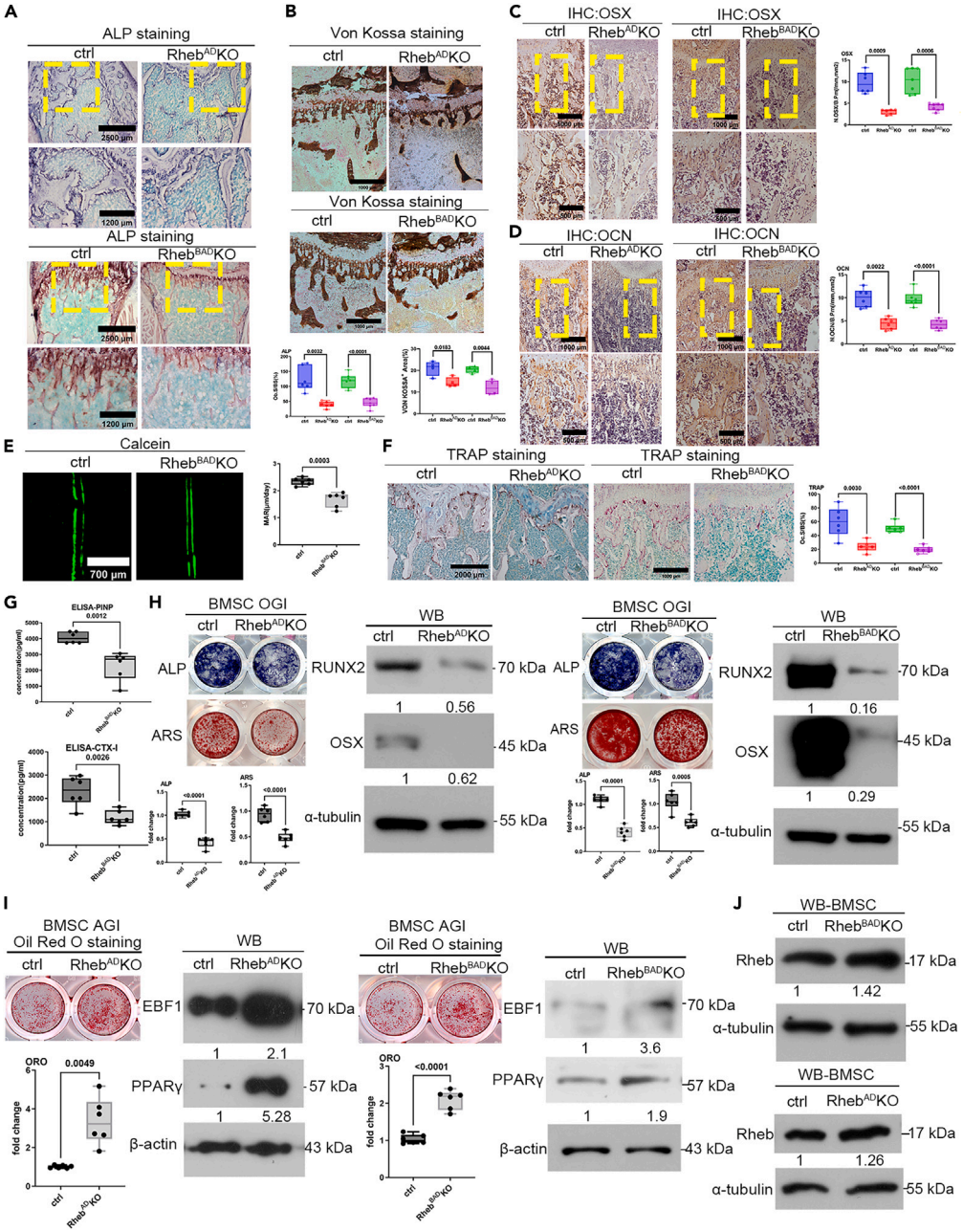

Figure 3. Rheb ablation in BAT led to reduced osteoblast differentiation *in vivo* and *ex vivo*

Distal femur sections of the control and *Rheb*^{AD} KO mice (upper panel), or control and *Rheb*^{BAD} KO mice (lower panel) were analyzed for osteogenesis by ALP staining (A), by Von Kossa staining (B), for the osteogenic markers OSX (C)) or OCN (D) by IHC staining, by calcein labeling (E), or for osteoclast differentiation by TRAP staining (F). Ob.S/BS, Osteoblasts surface to bone surface; MAR, mineral apposition rate; Oc.S/BS, osteoclasts surface to bone surface; N.OSX/B.Pm, OSX positive cell number over bone perimeter, and N·OCN/B.Pm, OCN positive cell number over bone perimeter.

(G) Serum Procollagen I N-Terminal Propeptide (PINP) and Cross Linked C-Telopeptide of Type I Collagen (CTX-I) were analyzed by ELISA. Primary BMSCs were isolated from the femoral medullary cavity of the control and *Rheb*^{AD} KO mice, or control and *Rheb*^{BAD} KO mice, cultured *in vitro*, and induced for osteoblastic (H) or adipocytic differentiation (I). The results were analyzed by ALP or Oil red O staining (left panel), respectively, as well as by WB assay for the indicated osteogenic or adipogenic markers (right panel).

(J) The expression of Rheb in primary undifferentiated BMSCs were analyzed by WB assay. Data are shown as box-and-whisker plots (with median and interquartile ranges) from max to min, with all data points shown. Analyses were performed as two-tailed unpaired t-test.

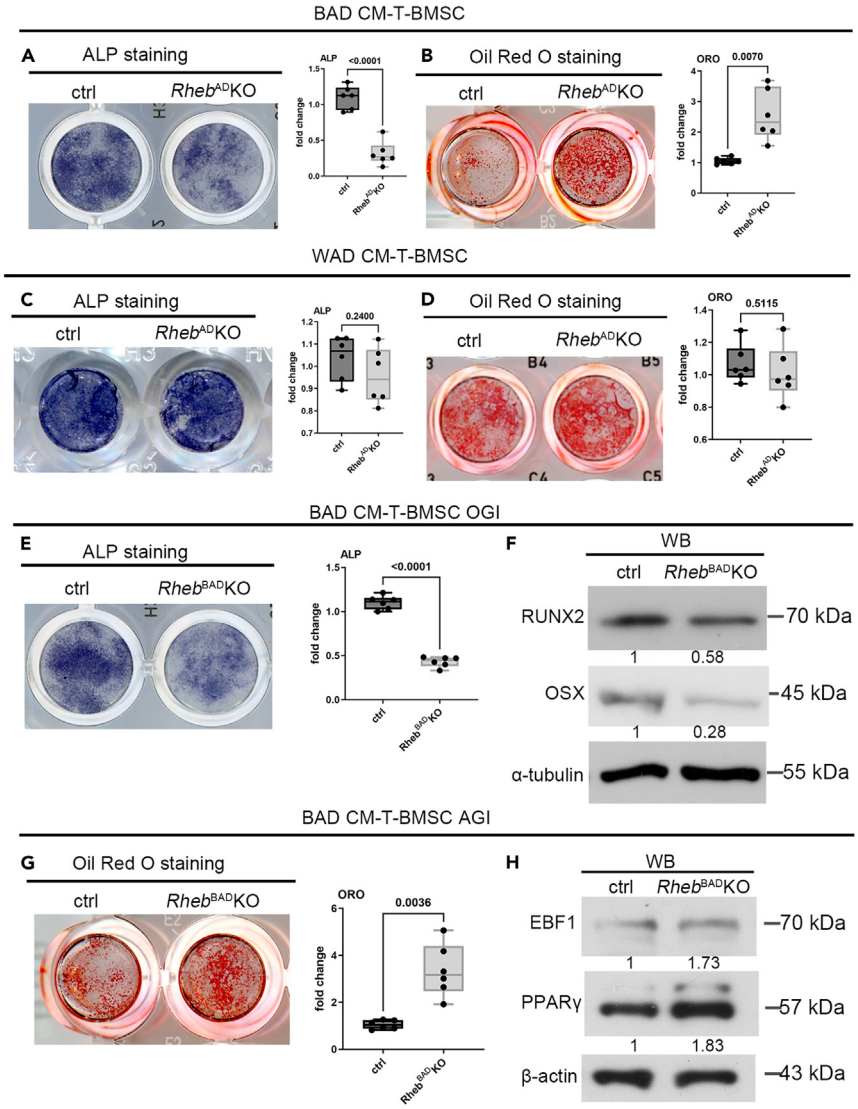

Figure 4. Brown but not white adipocytes from Rheb-ablated mice suppress osteoblast differentiation from BMSCs

Primary BMSCs were isolated from wild-type C57BL/6J mice, cultured *in vitro*, and treated with conditioned medium (CM) collected either from interscapular BADs (BAD CM-T-BMSC) (A, B), or from epididymal WADs (WAD CM-T-BMSC) (C, D) of control or *Rheb*^{AD} KO mice. These cells were induced to differentiate into osteoblasts (OB) or adipocytes (AD), followed by inspection with ALP (A, C) or Oil red O (B, D) staining, respectively. Primary wild-type BMSCs were also treated with CM collected from interscapular BADs of *Rheb*^{BAD} KO mice, induced for OB or AD differentiation. While OB differentiation was analyzed by ALP staining (E) or western blotting for the indicated OB markers (F), AD differentiation was observed by Oil red O (G) staining or western blotting for the indicated AD markers (H). Data are shown as box-and-whisker plots (with median and interquartile ranges) from max to min, with all data points shown. Analyses were performed as two-tailed unpaired t-test.

Transcription factor-binding-motif analysis of the upregulated genes in the BAT of *Rheb*^{BAD} KO mice using the i-cisTarget web tool[39] revealed that the p65 NF-κB (*RelA*) consensus motif is most highly enriched (Figure S10A). Additionally, p65 has been documented to bind the promoter of S100A8 and S100A9 to activate its transcription.[40] Thus, we hypothesized that p65 transactivates S100A8/A9 in BADs in response to Rheb depletion. As expected, the level of p65 NF-κB phosphorylation (S276, a hallmark of p65 transcriptional activity) was much higher in BADs of *Rheb*^{AD} KO and *Rheb*^{BAD} KO mice (Figures S10B and S10C) than in control mice. Consistently, Rheb-depleted primary BADs displayed a marked elevation of p65 phosphorylation level (Figures S10D and S10E), as shown by western blotting. Brown adipocytes can be induced from C2C12 cells (named thereafter C2C12 BADs) *in vitro* by supplementation of a retinoid X receptor agonist, bexarotene.[41,42] Conversely, simultaneous treatment of these C2C12 BADs with the NF-κB inhibitor QNZ or SN50 markedly blunted the effect of rapamycin on S100A8 expression and secretion (Figures S10F and S10G). Collectively, these data suggest that S100A8 stimulated by Rheb depletion is dependent on p65 NF-κB.

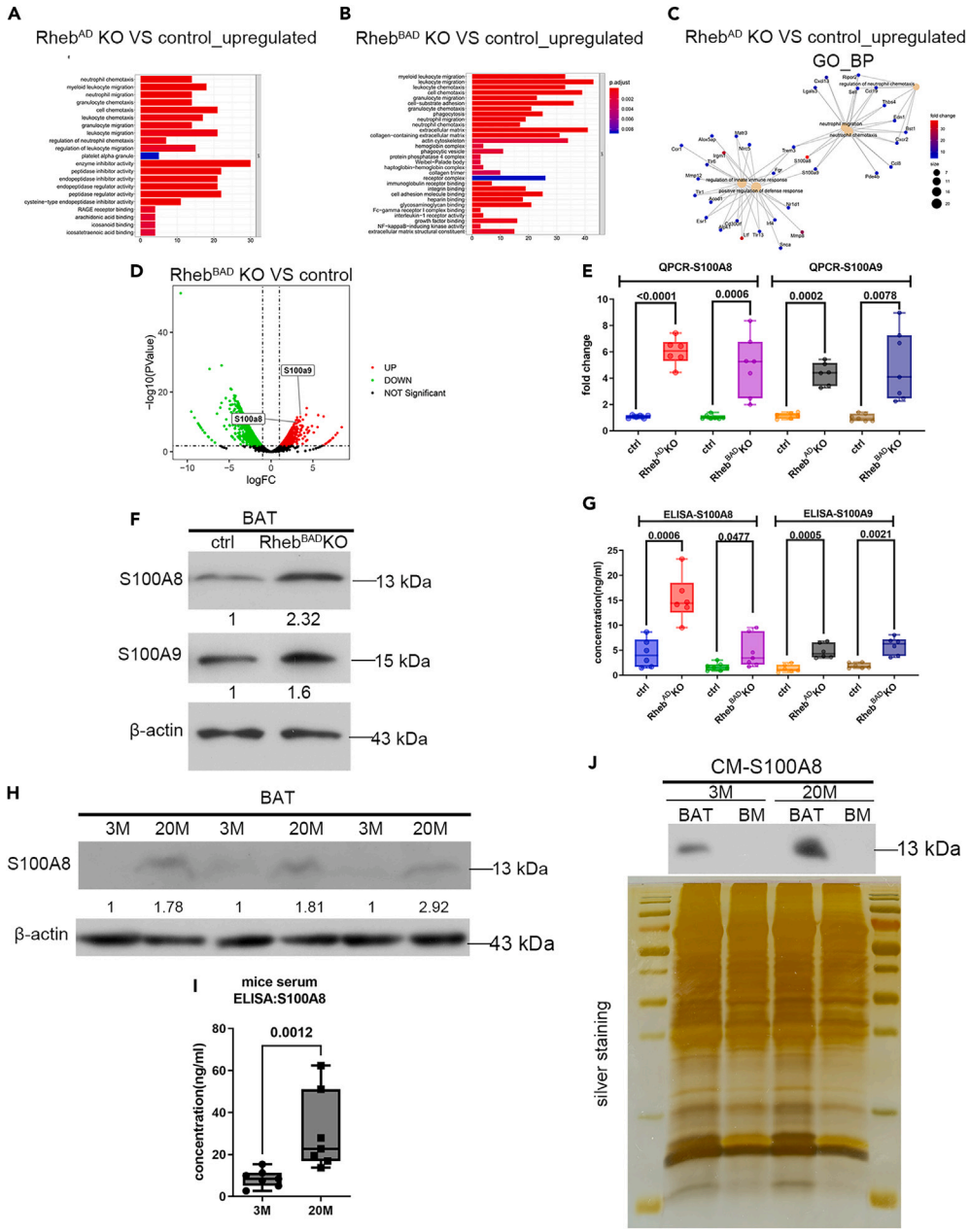

Figure 5. Loss of Rheb in BAT induces transcription and secretion of S100A8/A9

Interscapular BAT from either control or *Rheb*^{AD} KO (A), or from control or *Rheb*^{BAD} KO (B) mice, were used for transcriptome analysis by RNA-sequencing. The significantly upregulated genes were further subjected to gene ontology (GO) analysis. Detailed biological processes of the significantly upregulated genes in the *Rheb*^{AD} KO mice are shown as a CNET plot (C). (D) Significantly up- or downregulated genes (at least two-fold, $p < 0.01$) in the BAT of control or *Rheb*^{BAD} KO mice are shown as a volcano plot, with S100A8 and S100A9 labeled. S100A8 and S100A9 expression in the BAT of control or *Rheb*^{AD} KO (or control or *Rheb*^{BAD} KO) mice was analyzed by RT-qPCR (E) or western blotting (F).

(G) Serum S100A8 and S100A9 levels of these mice were determined by ELISA or western blotting. Interscapular BAT (H) or serum (I) of the 3-month and 20-month C57BL/6J mice were analyzed for S100A8 expression by western blotting.

(J) Conditional medium (CM) collected from interscapular BAT or bone marrow cells from these mice were analyzed for S100A8 by western blotting. Silver staining was used to assess equal loading. Data are shown as box-and-whisker plots (with median and interquartile ranges) from max to min, with all data points shown. Analyses were performed as two-tailed unpaired t-test.

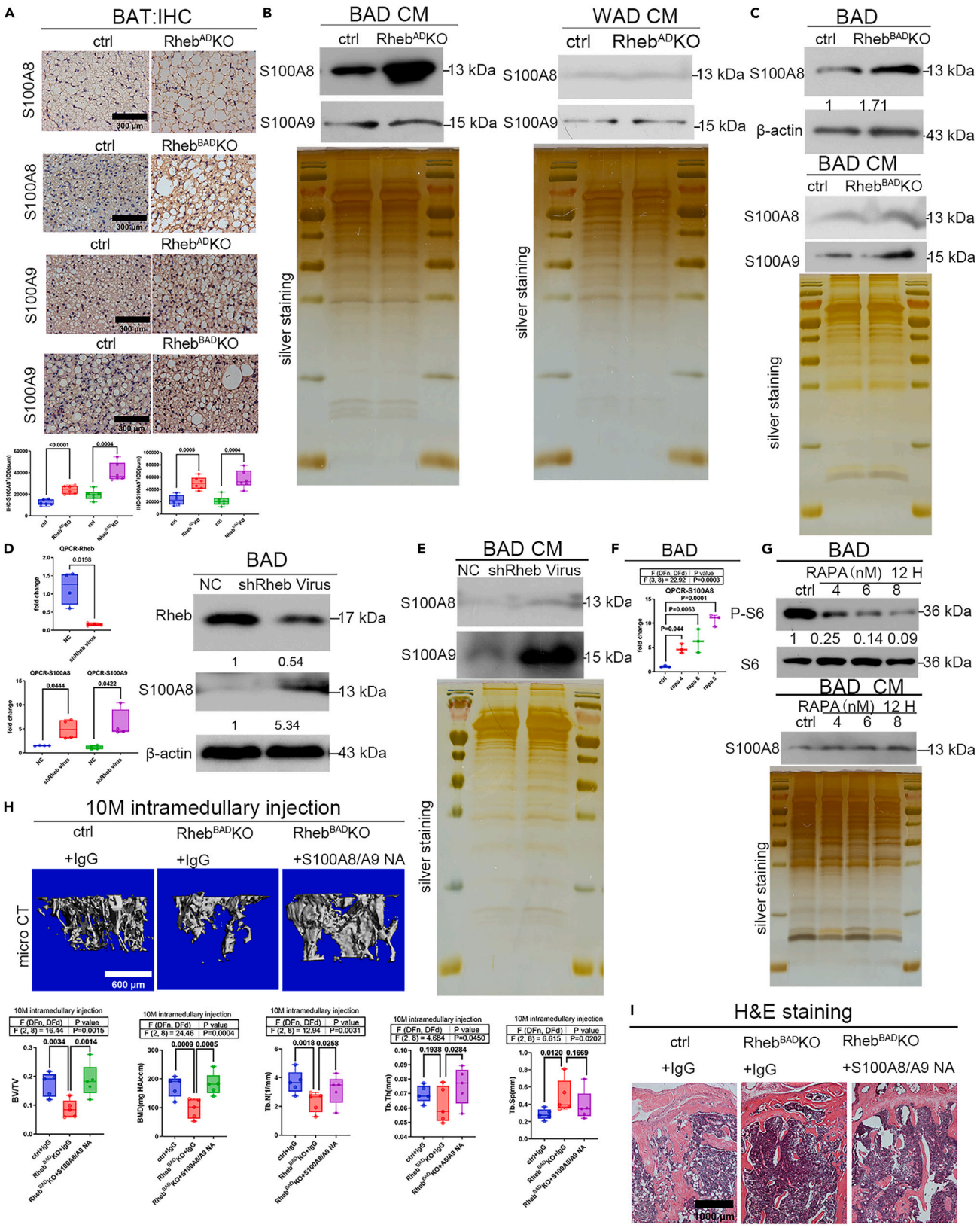
A
BAT:IHC
ctrl
RhebADKO
RhebBADKO
S100A8
S100A9
300 μm
B
BAD CM
WAD CM
S100A8
S100A9
13 kDa
15 kDa
silver staining
C
BAD
β-actin
43 kDa
1
1.71
D
QPCR-Rheb
0.0198
fold change
NC
shRheb virus
QPCR-S100A8
QPCR-S100A9
0.0444
0.0422
Rheb
17 kDa
0.54
5.34
E
NC
shRheb Virus
F
QPCR-S100A8
P=0.0001
P=0.0063
P=0.044
rapa 4
rapa 8
G
RAPA (nM)
12 H
P-S6
S6
36 kDa
0.25
0.14
0.09
H
10M intramedullary injection
+IgG
+S100A8/A9 NA
micro CT
600 μm
BV/TV
BMD(mg HA/ccm)
Tb.N(1/mm)
Tb.Th(mm)
Tb.Sp(mm)
I
H&E staining
1000 μm

Figure 6. Brown adipocytic S100A8/A9 mediates the effect of BAT Rheb loss on osteogenesis

(A) Interscapular BAT from either control or *Rheb*^{AD} KO, or from control or *Rheb*^{BAD} KO mice, were analyzed for S100A8 or S100A9 expression by immunohistochemistry. The conditional medium (CM) was collected from both interscapular BADs and epididymal WADs of the control and *Rheb*^{AD} KO mice (B), or from interscapular BADs of the control and *Rheb*^{BAD} KO mice (C). The cells were then lysed, followed by both the whole-cell lysates and CM analyzed for S100A8 and S100A9 expression by WB. Primary brown adipocyte progenitors (BPADs) from wild-type C57BL/6J mice were transfected with lentivirus carrying the control or Rheb shRNA and induced into mature BADs, followed by analysis of whole-cell or secreted S100A8 level via RT-qPCR (D) or WB (E), respectively. BPADs were induced into BADs and treated with various concentrations of rapamycin for 12 h, then analyzed for S100A8 expression via RT-qPCR (F) and WB (G). The efficiency of rapamycin treatment was assessed by monitoring phosphorylated S6 (S235/236) (G). S100A8/A9 neutralizing antibody was injected into the tibial medullary cavity of *Rheb*^{BAD} KO mice (10-month) every 3 days for 2 months, and the effects on bone formation were analyzed by 3D-microCT (H) or HE staining (I). Bone histomorphometric parameters of the tibiae were shown in the lower panel of (H). Data are shown as box-and-whisker plots (with median and interquartile ranges) from max to min, with all data points shown. Two-tailed unpaired t-test was used for two-group comparison; for comparison between multiple groups, one-way analysis of variance with multiple comparisons were used, followed by the Bonferroni post-hoc test for significance.

Brown adipocytic S100A8/A9 mediates the effect of BAT Rheb loss on osteogenesis

Since it has been reported that S100A8/A9 is derived mainly from myeloid cells including neutrophils or macrophages,[43–45] we next investigated whether BADs can also secrete S100A8/A9. Brown adipocytes in both *Rheb*^{BAD} KO and *Rheb*^{AD} KO mice showed markedly enhanced S100A8 and S100A9 expression (Figure 6A). Consistent with this notion, both lysates and culture medium of primary BADs isolated from *Rheb*^{AD} KO (Figure 6B) mice and *Rheb*^{BAD} KO mice (Figure 6C) displayed significantly higher S100A8 and S100A9 protein levels than that from their control littermates. To compare the contribution of BADs and myeloid cells in the release of S100A8/A9, BAT from the control or *Rheb*^{BAD} KO mice were fractioned into mature BADs and stromal-vascular fractions (SVF) and analyzed for the expression of S100A8/A9. In control mice, the baseline expression levels of S100A8 and S100A9 in the SVF fraction were slightly higher than those in mature BADs. In sharp contrast, mature BADs showed much higher S100A8 and S100A9 expression levels than SVF in Rheb^{BAD} KO mice (Figure S11A). Furthermore, in comparison with the control mice, *Rheb*^{BAD} KO mice showed similar number of total macrophages, M1 macrophages, and M2 macrophages (Figures S11B and S11C). Collectively, these results suggest that BADs are the main sources for S100A8/A9 secretion in *Rheb*^{BAD} KO mice.

Additionally, transfection of Rheb shRNA into primary BADs resulted in a marked increase in S100A8 and S100A9 expression and secretion, as revealed by RT-qPCR and WB analysis of the cell lysates (Figure 6D), as well as by WB analysis of the culture medium (Figure 6E). Further, treatment with rapamycin, a specific mTORC1 inhibitor, also increased S100A8 expression and secretion dose-dependently in primary BADs derived from wild-type C57BL/6J mice (Figures 6F and 6G) or C2C12 BADs (Figures S11D–S11F). In contrast, bone marrow-derived macrophages of *Rheb*$^{FL/FL}$ mice infected with adenovirus encoding *Cre* showed no significant alteration in the mRNA level of S100A8 (Figure S11G). Collectively, these results confirmed that Rheb depletion induces S100A8 expression and secretion in BADs *in vitro*, probably via inactivation of mTORC1.

To test whether S100A8/A9 is a factor suppressing bone formation downstream of Rheb loss in BADs, we explored several loss-of-function strategies to assess the effect of blocking S100A8/A9 on bone formation. Intramedullary injection of S100A8/9 neutralizing antibody markedly reversed the reduction of trabecular bone mass, BMD, and trabecular numbers in 10-month-old Rheb^{BAD} KO mice (Figures 6H and 6I). The reduction in OB differentiation of Rheb^{BAD} KO mice was also rescued (Figures S12A–S12C). OCs were also reduced by this treatment (Figure S12D), consistent with a previous finding that S100A8 stimulates OCs formation.[46] Likewise, tail-vein injection of S100A8/A9 neutralizing antibody had similar rescue effects on the reduction in bone mass and OB differentiation of *Rheb*^{BAD} KO mice (Figures S12E and S12F). Consistently, intramedullary treatment with S100A8/A9 neutralizing antibody for 2 months generated the similar effects in 5-month-old *Rheb*^{BAD} KO mice, which are at the early stage of age-related bone loss (Figures S12G–S12I). Further, S100A8/A9 neutralization in 5-month-old C57BL/6J mice and in 10-month-old C57BL/6J mice for 2 months led to significant increases in trabecular bone mass, trabecular number, and BMD (Figures S12J and S12K).

Sympathetic nerves release noradrenaline to promote BAT thermogenesis while repressing bone formation.[47] Recently, it was shown that this sympathetic nerve innervation in BAT was controlled by paracrine secretion of S100B by BADs.[48] Depletion of the *Rheb* gene in BAD did not alter serum level of noradrenaline (Figure S12L), suggesting that the Rheb-S100A8 axis may regulate bone formation independently of the sympathetic system.

In vitro, supplementation with S100A8/A9 neutralizing antibody blunted the suppressing or promoting effect of BAD CM from *Rheb*^{BAD} KO mice on OB or AD differentiation from BMSCs, respectively (Figures S13A and S13B). However, CM from S100A8-depleted primary BADs did not significantly enhance OB differentiation from BMSCs (Figures S13C and S13D), suggesting that the effects of BAD-derived S100A8 on osteogenesis are negligible in physiological conditions. Consistently, recombinant S100A8/A9 suppressed OB differentiation of primary BMSCs from wild-type C57BL/6J mice, C3H10T1/2 MSCs, as well as C2C12 stromal cells dose-dependently (Figures S13E–S13G), without compromising cell viability (Figures S13H–S13J).

S100A8/A9 inhibits OB differentiation of BMSCs through targeting toll-like receptor 4 (TLR4)

Previously-reported cell membrane receptors for S100A8/A9, TLR4, or receptor for advanced glycation end-products (RAGE)[49,50] in BMSCs, were analyzed by RT-qPCR. Interestingly, BMSCs showed a much higher TLR4 expression level than that of RAGE (Figure 7A). We next tested

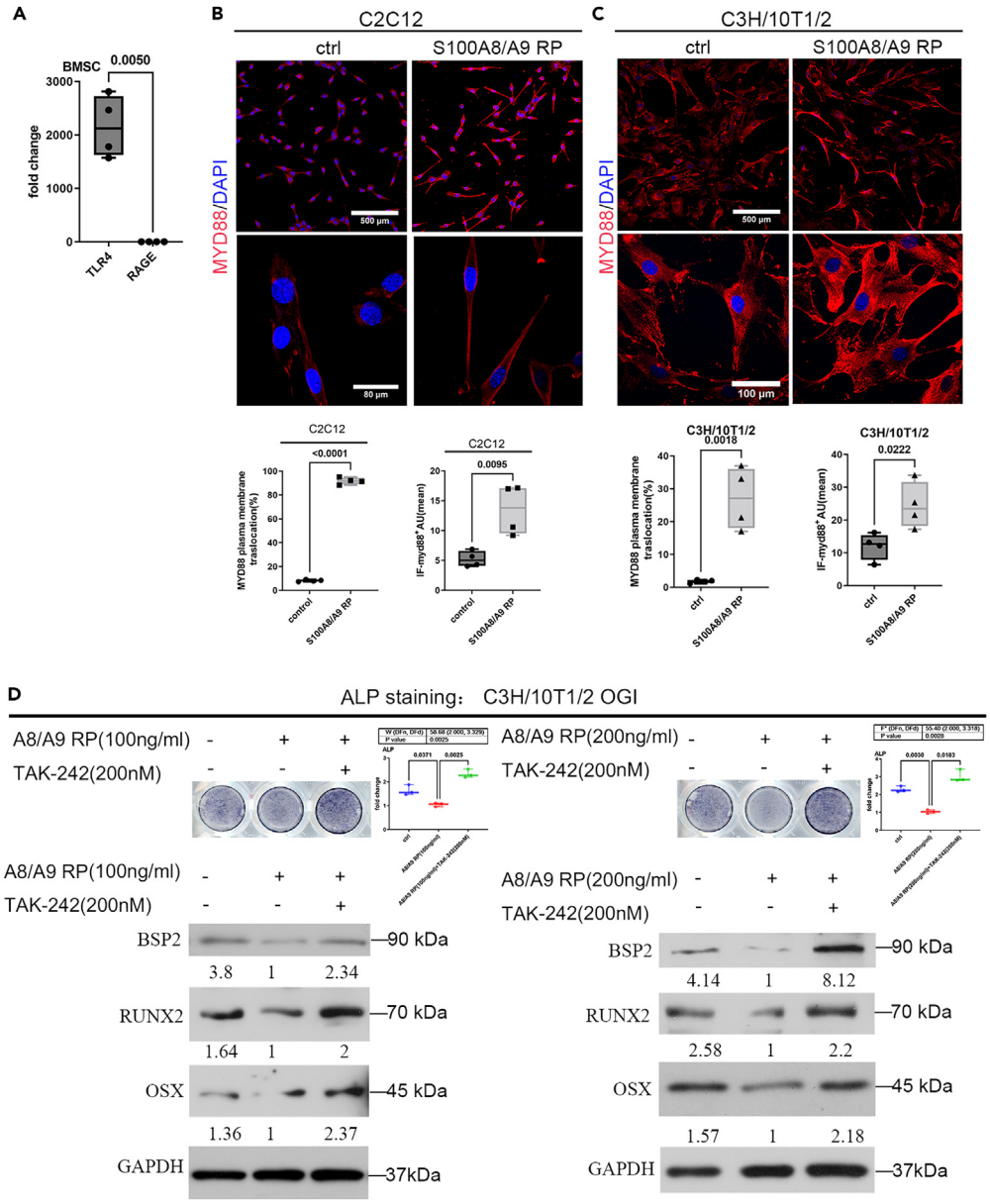

Figure 7. S100A8/A9 inhibits OB differentiation of BMSCs through targeting toll-like receptor 4 (TLR4)

(A) Expression of the S100A8/A9 receptor TLR4 and RAGE in primary BMSCs was analyzed by RT-qPCR. C2C12 stromal cells (B) and C3H10T1/2 MSCs (C) were treated with recombinant S100A8/A9 and analyzed for Myd88 expression and localization by confocal microscopy. Original magnification, ×200 or ×600; scale bar was shown as indicated. (D) C3H10T1/2 cells were treated with S100A8/A9 and TLR4 inhibitor TAK242 as indicated, followed by assay for OB differentiation by ALP staining (upper panel) and WB (lower panel). For comparisons between 2 groups, two-tailed unpaired t-tests were used. For comparisons between multiple groups, one-way analysis of variance with multiple comparisons were used, followed by the Bonferroni post-hoc test for significance. Data are shown as box-and-whisker plots (with median and interquartile ranges) from max to min, with all data points shown. Two-tailed unpaired t-test was used for two-group comparison; for comparison between multiple groups, one-way analysis of variance with multiple comparisons were used, followed by the Bonferroni post-hoc test for significance.

whether TLR4 in MSCs is activated upon S100A8/A9 treatment. Indeed, both C3H10T1/2 and C2C12 MSCs demonstrated fast Myd88 translocation to the plasma membrane, a well-known hallmark of TLR4 activation,[51,52] as well as a prominent elevation in its protein level in response to S100A8/A9 stimulation, as observed from fluorescence confocal microscopy (Figures 7B and 7C). Conversely, supplementation with the TLR4 inhibitor TAK242 dramatically reversed the suppressive effect of S100A8/A9 on OB differentiation of C3H10T1/2 MSCs (Figure 7D), further suggesting that S100A8/A9 may repress BMSC differentiation by targeting TLR4.

DISCUSSION

The endocrine role of BAT in bone development, homeostasis, and involution and the underlying mechanism remains largely unclear. In the current study, we provided *in vivo* evidence that batokines released from whitened BAT suppress osteogenesis remotely. Loss of Rheb in BAT results in release of batokines including S100A8/A9, which in turn activate TLR4-Myd88 signaling in BMSCs, preventing their OB differentiation while promoting AD differentiation (Graphical Abstract). Our data revealed a previously uncharacterized pathological role of dysfunctional BAT in remote inhibition of osteogenesis, through the action of batokines including S100A8/A9.

The activity of Rheb-mTOR signaling is modulated by both GTPase activity of Rheb and its expression level. Both reduction of TSC GAP activity and loss-of-function mutation of TSC promotes Rheb activity. On the contrary, low energy or DNA damage suppresses Rheb activity via activation of TSC.[44,53] Regulation of Rheb-mTOR signaling has been implicated in energy metabolism disorders. Mice with high-fat diet-induced obesity is associated with hyperactivation of Rheb-mTOR signaling.[54] Paradoxically, mice with ectopic Rheb expression in pancreatic β cells showed improved glucose tolerance and resistance to hyperglycemia induced by obesity.[55] While Rheb activates mTOR signaling to suppress lipolysis, it inhibits white-beige transformation of fat and thermogenesis in an mTORC1-independent but PDE45-CAMP-dependent mechanism,[56] further complicating the regulatory role of Rheb-mTOR in metabolism. In this regard, understanding tissue- or cell-type specific role(s) of Rheb-mTOR in these pathological conditions is of fundamental importance to perform targeted inhibition or activation of the pathway without side effects.

Combining the results from Rheb ablation in BAD only (*Ucp1-Cre*), or in both BAD and WAD (*Fabp4-Cre*), we demonstrated that Rheb-mTOR inactivation in BAT led to BAT malfunction, outburst of inflammatory batokines including S100A8/A9, and consequent reduction of osteogenesis. Although *Fabp4-Cre* was also shown to be expressed in macrophages besides adipocytes,[31] based on our previous results revealing that mTOR inactivation in macrophages (using *Lyz-Cre*) enhances osteoclastogenesis without altering osteogenesis,[57] it is less likely that nonspecific Rheb ablation in macrophages accounts for the osteopenic phenotype observed in $Rheb^{AD}$ KO mice. Ucp1 was reported to be a specific marker for BAD.[6] Consistently, *Ucp1-Cre* expression was only observed in BAD among the examined tissue/organs in this study. Importantly, SVF fraction of BAT from $Rheb^{BAD}$ KO showed no reduction in Rheb expression, suggesting that the osteopenic phenotype observed in $Rheb^{BAD}$ KO mice was specially caused by Rheb depletion in BAD. However, due to the observed Rheb depletion in beige depots, although to a lesser extent than the classical BAT, we cannot exclude the role of beige adipocytes in this BAT-bone crosstalk.

Consistent with the notion that activation of browning program in white adipocytes may support OB differentiation during bone development,[58] our results suggest that whitening of brown adipocytes driven by Rheb loss suppress trabecular bone formation, reduce its peak bone mass, and accelerates its involution. Resembling $Rheb^{BAD}$ KO and $Rheb^{AD}$ KO mice, aged wild-type mice displayed a significant increase of S100A8/A9 both in BAT and serum, concomitant with Rheb depletion and BAT whitening. This reflects the functional relevance of Rheb-S100A8/A9 axis in AOP, although the trabecular bone loss caused by deregulation of this axis does not faithfully phenocopy the latter. Additionally, these results reveal an evolutionary role of Rheb-mTOR in BAT-bone metabolism. It is likely that dysfunction of this signaling axis during aging drives the switch of BAT-bone coupling from an energetically efficient phenotype to an inefficient one, hence losing evolutionary advantage. However, it is unclear whether imbalance of Rheb-mTOR signaling in BAT will result in bone abnormalities in other metabolic disorders with BAT whitening, such as obesity and type 2 diabetes mellitus.[59,60]

Although S100A8/A9 is known to be secreted mainly by myeloid cells such as neutrophils and macrophages,[61,62] multiple lines of evidence suggest that S100A8/A9 derived from BADs, but not myeloid cells, may play a major role in the suppression of osteogenesis, at least in the initiating stage. (1) $Rheb^{BAD}$ and $Rheb^{AD}$ KO mice displayed markedly enhanced S100A8/A9 expression and secretion in primary BADs in comparison with their control littermates. (2) $Rheb^{BAD}$ mice exhibited markedly higher S100A8/A9 level in mature BAD fraction than in the SVF fraction of BAT, which mainly includes myeloid cells, lymphocytes, preadipocytes, and endothelial cells.[63,64] (3) Both primary BADs and induced C2C12 BADs with Rheb-mTOR inactivation showed markedly increased S100A8/A9 secretion *in vitro*. (4) Macrophages with *Rheb* knockout *in vitro* did not display significant alteration in S100A8/A9 expression. (5) There were far less infiltrating macrophages than BADs in the BAT (less than 5% of $CD45^+$ leukocytes and even lesser macrophages), which does not change during aging.[64] Additionally, no significant differences were observed in the number of either total, M1, or M2 macrophages between the control and Rheb knockout mice. (6) We further revealed whitened BAT of aged mice secrete much more S100A8 than bone marrow per se. Taken together, these data suggest that BAD may serve as one of the primary sources of S100A8/A9 secretion upon BAT dysfunction induced by Rheb-mTOR inactivation. Nevertheless, we cannot exclude that S100A8/A9 secretion from BAD may result in feedback secretion of itself from other cells, tissue, or organs and this feedback secretion may also contribute to maintain the suppression on osteogenesis. Interestingly, a very recent study revealed that bone marrow-derived pro-inflammatory $S100A8^+$ immune cells invade the BAT of male rats and mice and impair their sympathetic innervation and thermogenesis during aging.[65] Taken together with our findings, these data suggest a possible dual intercommunication role of S100A8 in the bone-BAT axis.

S100A8/A9 has been shown to enhance osteoclastic bone resorption[46] and aggravate osteoarthritis,[66,67] while its role in OB differentiation is unknown. However, our results did not show a prominent increase in OC numbers either in $Rheb^{AD}$ KO mice or $Rheb^{BAD}$ KO mice, suggesting that the bone loss in these mice cannot be attributed to the effect of S100A8/A9 on OCs. In fact, S100A8/A9 strongly suppresses OB differentiation from MSCs by targeting TLR4, the most abundant receptor for S100A8/A9 in MSCs. Supporting our data, TLR4 knockout accelerated bone healing after a skull lesion,[68] and MyD88 deficiency accelerated bone regeneration[69] and resistance to PAMP-induced bone loss.[70] Conversely, TLR4 activation in differentiating mouse primary Obs,[71] MC3T3-E1 osteoprogenitors,[72] or in MSCs[73] inhibited OB differentiation.

Taken together, our findings established a role of BAT in controlling bone formation, bearing important implications for disease conditions involving both BAT malfunction and bone loss, such as aging, anorexia nervosa, obesity, and type 2 diabetes. While this study expands knowledge of the secretory functions of BAT in whole-body metabolism, it will also provide a rationale for the treatment of osteoporosis by targeting the S100A8/A9-TLR4 axis.

Limitations of the study

In this study, both two Cre lines (*Ucp1-Cre* and *Fabp4-Cre*) are not inducible. Thus, the phenotypes of both knockout mice might be consequent on developmental disorders caused by Rheb loss in BAT. Using an inducible Cre line or fat-pad injection of AAV-Flex-shRheb to silence Rheb at selected time points may further corroborate the current findings. Interestingly, our finding that Rheb is necessary for UCP1 expression and browning maintenance in BAT is seemingly contradictory to the finding that Rheb inhibits beiging of WAT.[56] This inconsistence might be attributed to difference in different Cre lines (*Ucp1*-Cre VS *Adipoq*-Cre), but could also be attributed to regional regulatory mechanism of WAT and BAT. Analysis of the developmental and thermogenic program of WAT and BAT spatiotemporally, using cutting-edge technique such as stereo-seq will help uncover the underlying mechanism.

STAR★METHODS

Detailed methods are provided in the online version of this paper and include the following:

- KEY RESOURCES TABLE
- RESOURCE AVAILABILITY
  - Lead contact
  - Materials availability
  - Data and code availability
- EXPERIMENTAL MODEL AND STUDY PARTICIPANT DETAILS
  - Animal
  - Cell
- METHOD DETAILS
  - Primary culture of BMSCs
  - Osteogenic induction of BMSCs
  - Adipogenic induction of BMSCs
  - Isolation of primary brown and white adipocytes and collection of conditioned medium (CM)
  - Treatment of mouse BMSCs with conditioned medium (CM)
  - Isolation of mature brown adipocytes fraction (MAF) and stromal-vascular fractions (SVF)
  - Primary culture of bone marrow-derived macrophages (BMDMs)
  - Isolation, culture, and induction of primary brown preadipocytes (BPADs)
  - C3H/10T1/2 cell culture and osteogenic induction
  - C2C12 cell culture and induction
  - Cell treatment with S100A8/A9 recombinant protein (RP), rapamycin, and NF-κB inhibitor
  - Cell viability assay
  - mRNA array
  - RNA sequencing
  - Lentivirus infection
  - Cre-expressing adenovirus infection
  - Real time RT-PCR analysis
  - Western blotting, silver staining, and immunohistochemical assay
  - Secreted protein analysis by western blotting
  - Immunofluorescence
  - Micro-computed tomography (μCT) analyses
  - Frozen sections and ALP staining
  - Hard tissue sections
  - Blood biochemical studies
  - Enzyme-linked immunosorbent assay (ELISA)
  - S100A8/A9 neutralization *in vitro* and *in vivo*
  - Glucose tolerance test (GTT) and insulin tolerance test (ITT)
  - Cold and thermal neutrality exposure studies
  - Metabolic phenotyping
  - Bioinformatics analysis
- QUANTIFICATION AND STATISTICAL ANALYSIS

SUPPLEMENTAL INFORMATION

Supplemental information can be found online at https://doi.org/10.1016/j.isci.2024.108857.

ACKNOWLEDGMENTS

This work was supported by grants from the National Key R&D Program of China (Grant No. 2022YFC2502903), the National Natural Science Foundation of China (Grant No. 31771311, 81991511, 81871745, 81625015, 82002344), Guangzhou Municipal Science and Technology Project (Grant No. 201904010439), the Natural Science Foundation of Guangdong Province, China (2020A1515011035), the Guangdong Basic and Applied Basic Research Foundation (2019A1515110148), and the China Postdoctoral Science Foundation (2020M682801).

AUTHOR CONTRIBUTIONS

W.T., Z.C., Z.J., L.S., Z.Y., G.Y., Z.Y., Y.L., Z.S., and H.H. performed experiments; Z.Z. analyzed the microarray and RNA-sequencing data. Z.Z., B.X., and L.A. designed research, analyzed data, and wrote the manuscript.

DECLARATION OF INTERESTS

The authors declare that they have no competing interests.

Received: July 18, 2023
Revised: November 20, 2023
Accepted: January 5, 2024
Published: January 11, 2024

REFERENCES

1. Cannon, B., and Nedergaard, J. (2004). Brown adipose tissue: function and physiological significance. Physiol. Rev. *84*, 277–359.
2. Chondronikola, M., Volpi, E., Børsheim, E., Porter, C., Annamalai, P., Enerbäck, S., Lidell, M.E., Saraf, M.K., Labbe, S.M., Hurren, N.M., et al. (2014). Brown adipose tissue improves whole-body glucose homeostasis and insulin sensitivity in humans. Diabetes *63*, 4089–4099.
3. Orava, J., Nuutila, P., Lidell, M.E., Oikonen, V., Noponen, T., Viljanen, T., Scheinin, M., Taittonen, M., Niemi, T., Enerbäck, S., and Virtanen, K.A. (2011). Different metabolic responses of human brown adipose tissue to activation by cold and insulin. Cell Metab. *14*, 272–279.
4. Chondronikola, M., Volpi, E., Børsheim, E., Porter, C., Saraf, M.K., Annamalai, P., Yfanti, C., Chao, T., Wong, D., Shinoda, K., et al. (2016). Brown Adipose Tissue Activation Is Linked to Distinct Systemic Effects on Lipid Metabolism in Humans. Cell Metab. *23*, 1200–1206.
5. Gao, P., Jiang, Y., Wu, H., Sun, F., Li, Y., He, H., Wang, B., Lu, Z., Hu, Y., Wei, X., et al. (2020). Inhibition of Mitochondrial Calcium Overload by SIRT3 Prevents Obesity- or Age-Related Whitening of Brown Adipose Tissue. Diabetes *69*, 165–180.
6. Villarroya, F., Cereijo, R., Villarroya, J., and Giralt, M. (2017). Brown adipose tissue as a secretory organ. Nat. Rev. Endocrinol. *13*, 26–35.
7. Ruan, C.C., Kong, L.R., Chen, X.H., Ma, Y., Pan, X.X., Zhang, Z.B., and Gao, P.J. (2018). A(2A) Receptor Activation Attenuates Hypertensive Cardiac Remodeling via Promoting Brown Adipose Tissue-Derived FGF21. Cell Metab. *28*, 476–489.e5.
8. Kong, X., Yao, T., Zhou, P., Kazak, L., Tenen, D., Lyubetskaya, A., Dawes, B.A., Tsai, L., Kahn, B.B., Spiegelman, B.M., et al. (2018). Brown Adipose Tissue Controls Skeletal Muscle Function via the Secretion of Myostatin. Cell Metab. *28*, 631–643.e3.
9. Cereijo, R., Gavaldà-Navarro, A., Cairó, M., Quesada-López, T., Villarroya, J., Morón-Ros, S., Sánchez-Infantes, D., Peyrou, M., Iglesias, R., Mampel, T., et al. (2018). CXCL14, a Brown Adipokine that Mediates Brown-Fat-to-Macrophage Communication in Thermogenic Adaptation. Cell Metab. *28*, 750–763.e6.
10. Villarroya, J., Cereijo, R., Gavaldà-Navarro, A., Peyrou, M., Giralt, M., and Villarroya, F. (2019). New insights into the secretory functions of brown adipose tissue. J. Endocrinol. *243*, R19–R27.
11. Ponrartana, S., Aggabao, P.C., Hu, H.H., Aldrovandi, G.M., Wren, T.A.L., and Gilsanz, V. (2012). Brown adipose tissue and its relationship to bone structure in pediatric patients. J. Clin. Endocrinol. Metab. *97*, 2693–2698.
12. Bredella, M.A., Gill, C.M., Rosen, C.J., Klibanski, A., and Torriani, M. (2014). Positive effects of brown adipose tissue on femoral bone structure. Bone *58*, 55–58.
13. Cypess, A.M., Lehman, S., Williams, G., Tal, I., Rodman, D., Goldfine, A.B., Kuo, F.C., Palmer, E.L., Tseng, Y.H., Doria, A., et al. (2009). Identification and importance of brown adipose tissue in adult humans. N. Engl. J. Med. *360*, 1509–1517.
14. Khosla, S., and Riggs, B.L. (2005). Pathophysiology of age-related bone loss and osteoporosis. Endocrinol. Metab. Clin. North Am. *34*, 1015–1030.
15. Bredella, M.A., Fazeli, P.K., Freedman, L.M., Calder, G., Lee, H., Rosen, C.J., and Klibanski, A. (2012). Young women with cold-activated brown adipose tissue have higher bone mineral density and lower Pref-1 than women without brown adipose tissue: a study in women with anorexia nervosa, women recovered from anorexia nervosa, and normal-weight women. J. Clin. Endocrinol. Metab. *97*, E584–E590.
16. Ecklund, K., Vajapeyam, S., Feldman, H.A., Buzney, C.D., Mulkern, R.V., Kleinman, P.K., Rosen, C.J., and Gordon, C.M. (2010). Bone marrow changes in adolescent girls with anorexia nervosa. J. Bone Miner. Res. *25*, 298–304.
17. Bredella, M.A., Fazeli, P.K., Miller, K.K., Misra, M., Torriani, M., Thomas, B.J., Ghomi, R.H., Rosen, C.J., and Klibanski, A. (2009). Increased bone marrow fat in anorexia nervosa. J. Clin. Endocrinol. Metab. *94*, 2129–2136.
18. Gallego-Escuredo, J.M., Lamarca, M.K., Villarroya, J., Domingo, J.C., Mateo, M.G., Gutierrez, M.D.M., Vidal, F., Villarroya, F., Domingo, P., and Giralt, M. (2017). High FGF21 levels are associated with altered bone homeostasis in HIV-1-infected patients. Metabolism *71*, 163–170.
19. Saxton, R.A., and Sabatini, D.M. (2017). mTOR Signaling in Growth, Metabolism, and Disease. Cell *169*, 361–371.
20. Polak, P., Cybulski, N., Feige, J.N., Auwerx, J., Rüegg, M.A., and Hall, M.N. (2008). Adipose-specific knockout of raptor results in lean mice with enhanced mitochondrial respiration. Cell Metab. *8*, 399–410.
21. Lee, P.L., Tang, Y., Li, H., and Guertin, D.A. (2016). Raptor/mTORC1 loss in adipocytes causes progressive lipodystrophy and fatty liver disease. Mol. Metab. *5*, 422–432.
22. Li, L., Li, B., Li, M., Niu, C., Wang, G., Li, T., Król, E., Jin, W., and Speakman, J.R. (2017). Brown adipocytes can display a mammary basal myoepithelial cell phenotype *in vivo*. Mol. Metab. *6*, 1198–1211.
23. Claflin, K.E., Flippo, K.H., Sullivan, A.I., Naber, M.C., Zhou, B., Neff, T.J., Jensen-Cody, S.O., and Potthoff, M.J. (2022). Conditional gene targeting using UCP1-Cre mice directly targets the central nervous system beyond thermogenic adipose tissues. Mol. Metab. *55*, 101405.
24. Caron, A., Richard, D., and Laplante, M. (2015). The Roles of mTOR Complexes in

Lipid Metabolism. Annu. Rev. Nutr. *35*, 321–348.
25. Chakrabarti, P., English, T., Shi, J., Smas, C.M., and Kandror, K.V. (2010). Mammalian target of rapamycin complex 1 suppresses lipolysis, stimulates lipogenesis, and promotes fat storage. Diabetes *59*, 775–781.
26. Kazak, L., Chouchani, E.T., Jedrychowski, M.P., Erickson, B.K., Shinoda, K., Cohen, P., Vetrivelan, R., Lu, G.Z., Laznik-Bogoslavski, D., Hasenfuss, S.C., et al. (2015). A creatine-driven substrate cycle enhances energy expenditure and thermogenesis in beige fat. Cell *163*, 643–655.
27. Labbé, S.M., Mouchiroud, M., Caron, A., Secco, B., Freinkman, E., Lamoureux, G., Gélinas, Y., Lecomte, R., Bossé, Y., Chimin, P., et al. (2016). mTORC1 is Required for Brown Adipose Tissue Recruitment and Metabolic Adaptation to Cold. Sci. Rep. *6*, 37223.
28. Maliszewska, K., and Kretowski, A. (2021). Brown Adipose Tissue and Its Role in Insulin and Glucose Homeostasis. Int. J. Mol. Sci. *22*, 1530.
29. Urs, S., Harrington, A., Liaw, L., and Small, D. (2006). Selective expression of an aP2/Fatty Acid Binding Protein 4-Cre transgene in non-adipogenic tissues during embryonic development. Transgenic Res. *15*, 647–653.
30. Lee, K.Y., Russell, S.J., Ussar, S., Boucher, J., Vernochet, C., Mori, M.A., Smyth, G., Rourk, M., Cederquist, C., Rosen, E.D., et al. (2013). Lessons on conditional gene targeting in mouse adipose tissue. Diabetes *62*, 864–874.
31. Wolfrum, C., and Straub, L.G. (2019). Lessons from Cre-Mice and Indicator Mice. Handb. Exp. Pharmacol. *251*, 37–54.
32. Deng, J., Guo, Y., Yuan, F., Chen, S., Yin, H., Jiang, X., Jiao, F., Wang, F., Ji, H., Hu, G., et al. (2020). Autophagy inhibition prevents glucocorticoid-increased adiposity via suppressing BAT whitening. Autophagy *16*, 451–465.
33. Sellayah, D., and Sikder, D. (2014). Orexin restores aging-related brown adipose tissue dysfunction in male mice. Endocrinology *155*, 485–501.
34. Ferguson, V.L., Ayers, R.A., Bateman, T.A., and Simske, S.J. (2003). Bone development and age-related bone loss in male C57BL/6J mice. Bone *33*, 387–398.
35. Halloran, B.P., Ferguson, V.L., Simske, S.J., Burghardt, A., Venton, L.L., and Majumdar, S. (2002). Changes in bone structure and mass with advancing age in the male C57BL/6J mouse. J. Bone Miner. Res. *17*, 1044–1050.
36. Gillett, M.J., Vasikaran, S.D., and Inderjeeth, C.A. (2021). The Role of PINP in Diagnosis and Management of Metabolic Bone Disease. Clin. Biochem. Rev. *42*, 3–10.
37. Gunaratnam, K., Vidal, C., Gimble, J.M., and Duque, G. (2014). Mechanisms of palmitate-induced lipotoxicity in human osteoblasts. Endocrinology *155*, 108–116.
38. Pruenster, M., Vogl, T., Roth, J., and Sperandio, M. (2016). S100A8/A9: From basic science to clinical application. Pharmacol. Ther. *167*, 120–131.
39. Imrichová, H., Hulselmans, G., Atak, Z.K., Potier, D., and Aerts, S. (2015). i-cisTarget 2015 update: generalized cis-regulatory enrichment analysis in human, mouse and fly. Nucleic Acids Res. *43*, W57–W64.
40. Németh, J., Stein, I., Haag, D., Riehl, A., Longerich, T., Horwitz, E., Breuhahn, K., Gebhardt, C., Schirmacher, P., Hahn, M., et al. (2009). S100A8 and S100A9 are novel nuclear factor kappa B target genes during malignant progression of murine and human liver carcinogenesis. Hepatology *50*, 1251–1262.
41. Ghnaimawi, S., Baum, J., Liyanage, R., and Huang, Y. (2020). Concurrent EPA and DHA Supplementation Impairs Brown Adipogenesis of C2C12 Cells. Front. Genet. *11*, 531.
42. Nie, B., Nie, T., Hui, X., Gu, P., Mao, L., Li, K., Yuan, R., Zheng, J., Wang, H., Li, K., et al. (2017). Brown Adipogenic Reprogramming Induced by a Small Molecule. Cell Rep. *18*, 624–635.
43. Sreejit, G., Abdel Latif, A., Murphy, A.J., and Nagareddy, P.R. (2020). Emerging roles of neutrophil-borne S100A8/A9 in cardiovascular inflammation. Pharmacol. Res. *161*, 105212.
44. Wang, S., Song, R., Wang, Z., Jing, Z., Wang, S., and Ma, J. (2018). S100A8/A9 in Inflammation. Front. Immunol. *9*, 1298.
45. Shabani, F., Farasat, A., Mahdavi, M., and Gheibi, N. (2018). Calprotectin (S100A8/S100A9): a key protein between inflammation and cancer. Inflamm. Res. *67*, 801–812.
46. Grevers, L.C., de Vries, T.J., Vogl, T., Abdollahi-Roodsaz, S., Sloetjes, A.W., Leenen, P.J.M., Roth, J., Everts, V., van den Berg, W.B., and van Lent, P.L.E.M. (2011). S100A8 enhances osteoclastic bone resorption *in vitro* through activation of Toll-like receptor 4: implications for bone destruction in murine antigen-induced arthritis. Arthritis Rheum. *63*, 1365–1375.
47. Takeda, S., Elefteriou, F., Levasseur, R., Liu, X., Zhao, L., Parker, K.L., Armstrong, D., Ducy, P., and Karsenty, G. (2002). Leptin regulates bone formation via the sympathetic nervous system. Cell *111*, 305–317.
48. Zeng, X., Ye, M., Resch, J.M., Jedrychowski, M.P., Hu, B., Lowell, B.B., Ginty, D.D., and Spiegelman, B.M. (2019). Innervation of thermogenic adipose tissue via a calsyntenin 3β-S100b axis. Nature *569*, 229–235.
49. Sakaguchi, M., Yamamoto, M., Miyai, M., Maeda, T., Hiruma, J., Murata, H., Kinoshita, R., Winarsa Ruma, I.M., Putranto, E.W., Inoue, Y., et al. (2016). Identification of an S100A8 Receptor Neuroplastin-β and its Heterodimer Formation with EMMPRIN. J. Invest. Dermatol. *136*, 2240–2250.
50. Kovačić, M., Mitrović-Ajtić, O., Beleslin-Čokić, B., Djikić, D., Subotički, T., Diklić, M., Leković, D., Gotić, M., Mossuz, P., and Čokić, V.P. (2018). TLR4 and RAGE conversely mediate pro-inflammatory S100A8/9-mediated inhibition of proliferation-linked signaling in myeloproliferative neoplasms. Cell. Oncol. *41*, 541–553.
51. Barton, G.M., and Kagan, J.C. (2009). A cell biological view of Toll-like receptor function: regulation through compartmentalization. Nat. Rev. Immunol. *9*, 535–542.
52. Vogl, T., Tenbrock, K., Ludwig, S., Leukert, N., Ehrhardt, C., van Zoelen, M.A.D., Nacken, W., Foell, D., van der Poll, T., Sorg, C., and Roth, J. (2007). Mrp8 and Mrp14 are endogenous activators of Toll-like receptor 4, promoting lethal, endotoxin-induced shock. Nat. Med. *13*, 1042–1049.
53. Inoki, K., Zhu, T., and Guan, K.L. (2003). TSC2 mediates cellular energy response to control cell growth and survival. Cell *115*, 577–590.
54. Sciarretta, S., Zhai, P., Shao, D., Maejima, Y., Robbins, J., Volpe, M., Condorelli, G., and Sadoshima, J. (2012). Rheb is a critical regulator of autophagy during myocardial ischemia: pathophysiological implications in obesity and metabolic syndrome. Circulation *125*, 1134–1146.
55. Hamada, S., Hara, K., Hamada, T., Yasuda, H., Moriyama, H., Nakayama, R., Nagata, M., and Yokono, K. (2009). Upregulation of the mammalian target of rapamycin complex 1 pathway by Ras homolog enriched in brain in pancreatic beta-cells leads to increased beta-cell mass and prevention of hyperglycemia. Diabetes *58*, 1321–1332.
56. Meng, W., Liang, X., Chen, H., Luo, H., Bai, J., Li, G., Zhang, Q., Xiao, T., He, S., Zhang, Y., et al. (2017). Rheb Inhibits Beiging of White Adipose Tissue via PDE4D5-Dependent Downregulation of the cAMP-PKA Signaling Pathway. Diabetes *66*, 1198–1213.
57. Zhang, Y., Xu, S., Li, K., Tan, K., Liang, K., Wang, J., Shen, J., Zou, W., Hu, L., Cai, D., et al. (2017). mTORC1 Inhibits NF-κB/NFATc1 Signaling and Prevents Osteoclast Precursor Differentiation, In Vitro and In Mice. J. Bone Miner. Res. *32*, 1829–1840.
58. Rahman, S., Lu, Y., Czernik, P.J., Rosen, C.J., Enerback, S., and Lecka-Czernik, B. (2013). Inducible brown adipose tissue, or beige fat, is anabolic for the skeleton. Endocrinology *154*, 2687–2701.
59. Kotzbeck, P., Giordano, A., Mondini, E., Murano, I., Severi, I., Venema, W., Cecchini, M.P., Kershaw, E.E., Barbatelli, G., Haemmerle, G., et al. (2018). Brown adipose tissue whitening leads to brown adipocyte death and adipose tissue inflammation. J. Lipid Res. *59*, 784–794.
60. Shimizu, I., and Walsh, K. (2015). The Whitening of Brown Fat and Its Implications for Weight Management in Obesity. Curr. Obes. Rep. *4*, 224–229.
61. Sreejit, G., Abdel-Latif, A., Athmanathan, B., Annabathula, R., Dhyani, A., Noothi, S.K., Quaife-Ryan, G.A., Al-Sharea, A., Pernes, G., Dragoljevic, D., et al. (2020). Neutrophil-Derived S100A8/A9 Amplify Granulopoiesis After Myocardial Infarction. Circulation *141*, 1080–1094.
62. Scott, N.R., Swanson, R.V., Al-Hammadi, N., Domingo-Gonzalez, R., Rangel-Moreno, J., Kriel, B.A., Bucsan, A.N., Das, S., Ahmed, M., Mehra, S., et al. (2020). S100A8/A9 regulates CD11b expression and neutrophil recruitment during chronic tuberculosis. J. Clin. Invest. *130*, 3098–3112.
63. Ampem, G., and Röszer, T. (2019). Isolation and Characterization of Adipose Tissue Macrophages. Methods Mol. Biol. *1966*, 225–236.
64. Peterson, K.R., Flaherty, D.K., and Hasty, A.H. (2017). Obesity Alters B Cell and Macrophage Populations in Brown Adipose Tissue. Obesity *25*, 1881–1884.
65. Feng, X., Wang, L., Zhou, R., Zhou, R., Chen, L., Peng, H., Huang, Y., Guo, Q., Luo, X., and Zhou, H. (2023). Senescent immune cells accumulation promotes brown adipose tissue dysfunction during aging. Nat. Commun. *14*, 3208.
66. Zreiqat, H., Belluoccio, D., Smith, M.M., Wilson, R., Rowley, L.A., Jones, K., Ramaswamy, Y., Vogl, T., Roth, J., Bateman, J.F., and Little, C.B. (2010). S100A8 and S100A9 in experimental osteoarthritis. Arthritis Res. Ther. *12*, R16.
67. Schelbergen, R.F.P., de Munter, W., van den Bosch, M.H.J., Lafeber, F.P.J.G., Sloetjes, A., Vogl, T., Roth, J., van den Berg, W.B., van der Kraan, P.M., Blom, A.B., and van Lent, P.L.E.M. (2016). Alarmins S100A8/S100A9 aggravate osteophyte formation in experimental osteoarthritis and predict osteophyte progression in early human

symptomatic osteoarthritis. Ann. Rheum. Dis. *75*, 218–225.

68. Wang, D., Gilbert, J.R., Taylor, G.M., Sodhi, C.P., Hackam, D.J., Losee, J.E., Billiar, T.R., and Cooper, G.M. (2017). TLR4 Inactivation in Myeloid Cells Accelerates Bone Healing of a Calvarial Defect Model in Mice. Plast. Reconstr. Surg. *140*, 296e–306e.
69. Martino, M.M., Maruyama, K., Kuhn, G.A., Satoh, T., Takeuchi, O., Müller, R., and Akira, S. (2016). Inhibition of IL-1R1/MyD88 signalling promotes mesenchymal stem cell-driven tissue regeneration. Nat. Commun. *7*, 11051.
70. Madeira, M.F.M., Queiroz-Junior, C.M., Cisalpino, D., Werneck, S.M.C., Kikuchi, H., Fujise, O., Ryffel, B., Silva, T.A., Teixeira, M.M., and Souza, D.G. (2013). MyD88 is essential for alveolar bone loss induced by Aggregatibacter actinomycetemcomitans lipopolysaccharide in mice. Mol. Oral Microbiol. *28*, 415–424.
71. Bandow, K., Maeda, A., Kakimoto, K., Kusuyama, J., Shamoto, M., Ohnishi, T., and Matsuguchi, T. (2010). Molecular mechanisms of the inhibitory effect of lipopolysaccharide (LPS) on osteoblast differentiation. Biochem. Biophys. Res. Commun. *402*, 755–761.
72. Liu, Y.H., Huang, D., Li, Z.J., Li, X.H., Wang, X., Yang, H.P., Tian, S.P., Mao, Y., Liu, M.F., Wang, Y.F., et al. (2016). Toll-like receptor-4-dependence of the lipopolysaccharide-mediated inhibition of osteoblast differentiation. Genet. Mol. Res. *15*.
73. Chen, X., Zhang, Z.Y., Zhou, H., and Zhou, G.W. (2014). Characterization of mesenchymal stem cells under the stimulation of Toll-like receptor agonists. Dev. Growth Differ. *56*, 233–244.
74. Zou, J., Zhou, L., Du, X.X., Ji, Y., Xu, J., Tian, J., Jiang, W., Zou, Y., Yu, S., Gan, L., et al. (2011). Rheb1 is required for mTORC1 and myelination in postnatal brain development. Dev. Cell *20*, 97–108.
75. Liu, L., Zheng, L.D., Donnelly, S.R., Emont, M.P., Wu, J., and Cheng, Z. (2017). Isolation of Mouse Stromal Vascular Cells for Monolayer Culture. Methods Mol. Biol. *1566*, 9–16.

STAR★METHODS

KEY RESOURCES TABLE

REAGENT or RESOURCE	SOURCE	IDENTIFIER
Antibodies		
RHEB	Abcam	CAT#ab97896; RRID: AB_GR247594-4
Phospho-S6 (Ser235/236)	Cell Signaling Technology	CAT#2211S; RRID:AB_21
S6	Cell Signaling Technology	CAT#2317; RRID:AB_13
BSP2	Cell Signaling Technology	CAT#5468S ; RRID:AB_1
OSX	Abcam	CAT#ab22552; RRID:AB_GR3303054-1
RUNX2	Abclonal	CAT#A2851; RRID:AB_0080960102
PPARGC1A	Abclonal	CAT#A12348; RRID:AB_1154940303
PRDM16	Abcam	CAT#ab106410 ; RRID:AB_GR3230021-6
UCP1	proteintech	CAT#23673-1-AP; RRID:AB_00054446
EBF1	proteintech	CAT#14159-1-AP; RRID:AB_00005551
PPARγ	Cell Signaling Technology	CAT#2435S; RRID:AB_4
S100A8	Abclonal	CAT#A1688; RRID:AB_3507362001
P65	Abclonal	CAT#A10609; RRID:AB_9410609001
Phospho-P65(S276)	Abclonal	CAT#AP0123; RRID:AB_3560807218
β-actin	Affinity	CAT#AF7018; RRID:AB_12W2944
GAPDH	Beijing Ray Antibody Biotech	CAT#RM2002 RRID:Z0622
α-tubulin	Beijing Ray Antibody Biotech	CAT#RM2007 RRID:Z0305
myd88	Abclonal	CAT#A0980; RRID:AB_1602930402
BGLAP(OCN)	Abclonal	CAT#A6205; RRID:AB_3561388104
F4/80	Abcam	CAT#ab6640; RRID:GR3394048-1
INOS	Abcam	CAT#ab15323; RRID:GR3356847-1
CD206	R&D	CAT#AF2535-SP;RRID:WFT0319102
perilipin	Cell Signaling Technology	CAT#9349;RRID: AB_5
S100A9	proteintech	CAT#26992-1-AP; RRID:00063845
HSL	Abclonal	CAT#A15686;RRID:5500023058
P-HSL(S563)	Abclonal	CAT#AP0851;PRID:2158340301
Bacterial and virus strains		
Rheb Lentivirus	Genechem	5′-GCCAATTTGTTGATTCCTA-3′
Negative control (NC) Lentivirus	Genechem	contract number: GIDL0229913
S100A8 Lentivirus	Genechem	5′-CAACCTCATTGATGTCTACCA-3′
Ad-Cre (Cre-expressing adenovirus)	Genechem	contract number: GCD0299190
Chemicals, peptides, and recombinant proteins		
Rapamycin	MedChemExpress, MCE	CAT#HY-10219
S100A8/A9 neutralizing antibody	biolegend	CAT#697504
IgG antibody	biolegend	CAT#409306
SN50	MCE	CAT#HY-P0151
QNZ	Selleck	CAT#EVP4593
S100A8/A9 recombinant protein	R&D	CAT#8916-S8-050
TAK-242	Apexbio	CAT#A3850

(*Continued on next page*)

Continued

REAGENT or RESOURCE	SOURCE	IDENTIFIER
collagenase I digestion	Gibco	CAT#17100017
macrophage colony-stimulating factor	R&D	CAT#416-ML-010
forskolin (fsk)	selleck	CAT#66575-29-9
Bexarotene	Selleck	CAT#S2098-50mg
RNAiso Plus	TaKaRa	CAT#9109
metafectene pro	biontex	CAT#biontex
3,3′,5-Triiodo-L-thyronine (T3) solution	Sigma-Aldrich	CAT#T-074-1ML
DAPI	Fisher Scientific	CAT#D1306
α-MEM	Gibco	CAT#C12571500BT
Fetal bovine serum	Gibco	CAT#10099-141
DAB substrate Kit	Zsbio	CAT#ZLI-9305
MEM	Gibco	CAT#11095-080
RPMI 1640 Medium	Biological Industries	CAT#01-100-1AC
glutamax	GENOM2002	CAT#GNM-21051
sodium pyruvate	GENOM2002	CAT#GNM-11444
β-glycerol phosphate	Sigma-Aldrich	CAT#G9422
isobutylmethylxanthine	Sigma-Aldrich	CAT#I5879-100MG
All-trans retinoic acid	Sigma-Aldrich	CAT#R2625
dexamethasone	Sigma-Aldrich	CAT#D4902
Alexa 594 donkey anti-rabbit	Invitrogen	Cat #A21207
Indomethacin	Sigma-Aldrich	CAT#I7378-5G
rosiglitazone	Sigma-Aldrich	CAT#R2408
Insulin	Sigma-Aldrich	CAT#91077C
calcein	Sigma-Aldrich	CAT#c0875
Oil Red O	Sigma-Aldrich	CAT#O0625
Critical commercial assays		
Von Kossa staining kit	Abcam	CAT#ab150687
LEUKOCYTE ACID PHOSPHATASE(TRAP) KIT	Sigma-Aldrich	CAT#387A-1KT
Fast Silver Stain kit	Beyotime	CAT#P00175
PINP ELISA kit	Elabscience	CAT#E-EL-M0233c
CTX-1 ELISA kit	Cloud-clone	CAT#CEA665Mu
circulating glycerol kit	GEMIC	CAT#XFP17067
circulating free fatty acids kit	Solarbio	CAT# BC0595
ALP staining kit	Beyotime	CAT#C3206
Cell Counting Kit-8	Dojindo	CAT#CK04-500T
mouse leptin ELISA kit	Elabscience	CAT#E-EL-M3008
mouse S100A9 ELISA kit	Elabscience	CAT#E-EL-M3049
mouse S100A8 ELISA kit	Elabscience	CAT#E-EL-M1343c
Mouse Noradrenaline, NA ELISA Kit	CUSABIO	CAT#CSB-E07870m
PrimeScriptTM RT reagent Kit	TaKaRa	CAT#RR047A
Real-time quantitative PCR	TaKaRa	CAT#RR420A
Deposited data		
GSE183207	GEO	https://www.ncbi.nlm.nih.gov/geo/query/acc.cgi?acc=GSE183207

(*Continued on next page*)

Continued

REAGENT or RESOURCE	SOURCE	IDENTIFIER
GSE186094	GEO	https://www.ncbi.nlm.nih.gov/geo/query/acc.cgi?acc=GSE186094
Experimental models: Cell lines		
C3H/10T1/2	ATCC	CAT#CCL-226
C2C12	ATCC	CAT#CRL-1772
Experimental models: Organisms/strains		
UCP1-Cre mice (C57BL/6J)	Beijing Biocytogen	Stock number: 110134
Fabp4-Cre mice (C57BL/6J)	Beijing Biocytogen	Stock number: 110152
Rheb-fl/fl mice (C57BL/6J)	the West China Center of Medical Sciences,Sichuan University	A gift from Sichuan University
mtmg mice(C57BL/6J)	The Jackson Laboratory	Stock number: 007676
Oligonucleotides		
See Table S1 for the primers sequences	This paper	N/A
Software and algorithms		
ImagePro Plus 7	Media Cybernetics, Inc, Rockville, Maryland USA	https://www.mediacy.com/imageproplus
GraphPad Prism 9.5	GraphPad Software	https://www.graphpad.com/
Image J	National Institutes of Health (NIH)	https://imagej.nih.gov/ij/
ClusterProfiler	Guangchuang Yu's Lab, China	http://www.bioconductor.org/packages/release/bioc/html/clusterProfiler.html
enrichplot Bioconductor R	Guangchuang Yu's Lab, China	http://www.bioconductor.org/packages/release/bioc/html/enrichplot.html
Other		
Ctrl / *Rheb*^{BAD} KO mice	1 month/ 2 months/ 4 months/ 7 months/12 months/ 13 months	N/A
Ctrl / *Rheb*^{AD} KO mice	1 month/ 2 months/ 4 months	N/A
mT/mG mice	2 months	N/A
C57BL/6J mice	1 day/1 month/ 3 months/ 7 months/ 12 months/20 months	N/A

RESOURCE AVAILABILITY

Lead contact

Further information and requests for reagents and resources should be directed to and will be fulfilled by the lead contacts, Zhipeng Zou (zzp@smu.edu.cn).

Materials availability

This study did not generate new unique reagents.

Data and code availability

- mRNA and RNA-sequencing data has been submitted to GEO: https://www.ncbi.nlm.nih.gov/geo/query/acc.cgi?acc=GSE183207 and https://www.ncbi.nlm.nih.gov/geo/query/acc.cgi?acc=GSE186094. These accession numbers for the datasets are listed the "deposited data" section in the key resources table.
- This paper does not report original code.
- Any additional information required to reanalyze the data reported in this paper is available from the lead contact upon request.

EXPERIMENTAL MODEL AND STUDY PARTICIPANT DETAILS

Animal

Animal studies were approved by the Ethical Committee for Animal Research of Southern Medical University, and conducted according to guidelines from the Ministry of Science and Technology of China. *Rheb*$^{FL/FL}$ mice[74] were a gift from the West China Center of Medical Sciences, Sichuan University. *Fabp4-Cre* mice and *Ucp1-Cre* mice were both purchased from Beijing Biocytogen. Mice lacking *Rheb* in the adipocyte lineage were generated by mating *Rheb*$^{FL/FL}$ mice with *Fabp4-Cre* conditional knockout mice. Mice lacking *Rheb* in the brown adipocyte lineage were generated by mating *Rheb*$^{FL/FL}$ mice with *Ucp1-Cre* conditional knockout mice. The resulting *Fabp4-Cre*; *Rheb*$^{FL/FL}$ mice and *Ucp1-Cre*; Rheb$^{FL/FL}$ were hemizygous for the *Fabp4-Cre* or *Ucp1-Cre* and homozygous for the floxed *Rheb* allele. Co-housed *Rheb*$^{FL/FL}$ littermates were used as controls for all experiments. *ROSA26*$^{mT/mG}$ mice (Stock No. 007676) were purchased from the Jackson Laboratories (Bar Harbor, ME, USA). To generate *Ucp1-Cre*; *ROSA26*$^{mTmG/+}$ animals, heterozygous *Ucp1-Cre* males were bred to homozygous mTmG (*ROSA26*$^{mTmG/mTmG}$) female mice. Genotyping was performed using genomic DNA isolated from tail biopsies, and the primers used are shown in the Table S1. All animals were backcrossed for 10 generations onto the C57BL/6J background. Only male mice were used. C57BL/6J mice (newborns, 4–5 weeks old, 3 months old, 5 months old, 10 months old or 20 months old) were purchased from the Laboratory Animal Center of Southern Medical University (Guangzhou, China). Mice were housed in plastic cages at controlled temperatures of 22 $\pm$ 1°C, on a 12-h light/12-h dark cycle, with lights on from 06:00–18:00. Standard rodent chow and water were provided *ad libitum* throughout the study period. Before microCT or histological analysis, the mice were euthanized by cervical dislocation.

Cell

BMSC were isolated from the femora and tibiae of 4-6-week-old mice. Primary bone marrow-derived macrophages (BMDMs) were isolated from the femora and tibiae of 1-month-old *Rheb*$^{FL/FL}$ mice. Brown preadipocytes (BPADs) were isolated from interscapular BAT of neonatal mice. C2C12 myoblasts and C3H/10T1/2 mesenchymal stem cell were purchased from the American Type Culture Collection (ATCC). The cells were cultured in a humidified incubator at 37°C with 5% CO_2. Cell lines were not authenticated internally. All cells were routinely tested and confirmed to be free of mycoplasma (YK-DP-20, Ubigene Biosciences, Guangzhou, China).

METHOD DETAILS

Primary culture of BMSCs

Tibia and femur bones were harvested from 4-6-week-old mice. Briefly, the tissues around the bone were removed, and sterile PBS was syringed into the medullary cavity to flush out the bone marrow. The cell suspensions were then collected and centrifuged at 800 g for 5 min, with the pellets resuspended and cultured with complete medium consisting of α-MEM (C12571500BT, Gibco, Grand Island, NY, USA), 10% FBS (10099-141, Gibco), 1% penicillin and 1% streptomycin (15140-122, Gibco). BMSCs were cultured for 2 days and then washed to remove non-adherent cells and supplied with fresh α-MEM complete medium, with medium renewal every 2 days.

Osteogenic induction of BMSCs

After approximately 7 days post seeding, the primary BMSCs were switched into osteogenic medium (OGI, containing 10 nM dexamethasone, 10 mM β-glycerophosphate, and 50 μM ascorbic acid in α-MEM containing 10% FBS), or recombinant bone morphogenic protein 2 (BMP2, 300 ng/mL) to induce osteoblast differentiation. After osteogenic induction for 14 days, cells were fixed and subjected to ALP staining (C3206, Beyotime, Shanghai, China). After osteogenic induction for 21 days, the cells were subjected to alizarin red staining (ARS) (G1452, Solarbio, China).

Adipogenic induction of BMSCs

After 7 days post seeding, the primary BMSCs were changed into adipogenic induction medium (α-MEM supplemented with 10% FBS, 1 μM dexamethasone, 10 μg/mL insulin, 0.5 mM 3-isobutyl-1-methylxanthine, 10 μM rosiglitazone and 200 μM indomethacin). Three days after cells reached 100% confluence, the BMSCs were switched to maintenance medium (10% FBS α-MEM containing 5 μg/mL insulin and 10 nM dexamethasone). At 14 days post induction, cells were fixed and stained with oil red O (1052300025, Sigma-Aldrich, St Louis, MO, USA) according to standard protocols.

Isolation of primary brown and white adipocytes and collection of conditioned medium (CM)

Brown adipocytes and white adipocytes were isolated from interscapular BAT and white adipose tissue of 1-month-old mice, respectively, following a tissue extraction and 0.1% collagenase I digestion (17100017, Gibco) procedure. After digestion, the mixture was filtered through a 250-μm gauge mesh into a 50 mL conical polypropylene tube and allowed to stand for 2–3 min for the adipocytes to float to the top. The subnatant containing the collagenase solution was removed using a long needle and syringe, then 10 mL of adipocyte wash buffer (Krebs Ringer Bicarbonate HEPES buffer, containing 10 mM sodium bicarbonate, 30 mM HEPES and 500 nM adenosine, pH 7.4, supplemented with 3%(w/v) fatty acid-free bovine albumin fraction V) was added to the adipocytes and allowed to stand for 2–3 min. The subnatant was then removed once again and 10 mL of adipocyte wash buffer was added. The wash procedure was repeated three times, then the adipose cell suspension was centrifuged at 800 rpm for 30 s. After removing and discarding the subnatant, the upper floating layer of adipocytes was

taken and cultured with medium containing 10% heat-inactivated FBS in one well of a 12-well plate. After 24 h, conditioned medium (CM) was collected from BADs and WADs.

Treatment of mouse BMSCs with conditioned medium (CM)

BMSCs from wild-type C57BL/6J mice were plated into 24-well plates containing α-MEM with 10% FBS (10099-141, Gibco), 1% penicillin and 1% streptomycin. These BMSCs were treated with 10% CM (either heated at 95°C for 10 min or not) from BADs or WADs of the control and *Rheb*^{AD} KO mice, or from BADs of the control and *Rheb*^{BAD} KO mice 36 h before reaching complete confluence. After 36h, BMSCs were switched to osteogenic/adipogenic induction medium and cultured for 7 days, then either fixed and stained with ALP/Oil Red O, or lysed for total protein extraction and western blotting.

Isolation of mature brown adipocytes fraction (MAF) and stromal-vascular fractions (SVF)

MAF and SVF were isolated from interscapular BAT of 1-month-old mice, following a tissue extraction and 0.1% collagenase I digestion (17100017, Gibco) procedure as documented elsewhere.[9,75] After centrifuging for 5 min at 600g, mature BADs in the upper floating layer were collected for total RNA extraction. After further removal of brown preadipocytes, the resulting stromal vascular fractions were also harvested for total RNA extraction.

Primary culture of bone marrow-derived macrophages (BMDMs)

Primary bone marrow-derived macrophages (BMDMs) were isolated from the femora and tibiae of 1-month-old *Rheb*$^{FL/FL}$ mice. Bone marrow cells were flushed out and treated with erythrocyte lysis buffer to remove erythrocytes. The resulting cells containing macrophage/monocyte precursors were differentiated in RPMI 1640 Medium (01-100-1AC, Biological Industries) supplemented with 10% heat-inactivated FBS (10099-141, Gibco), 1% penicillin, 1% streptomycin, and 10 ng/ml macrophage colony stimulating factor (416-ML-010, R&D Systems) for 48h.

Isolation, culture, and induction of primary brown preadipocytes (BPADs)

Brown preadipocytes (BPADs) were isolated from interscapular BAT of neonatal mice by following a tissue extraction and 0.1% collagenase I digestion procedure. When BPADs grow to 100% confluence, the medium was changed to induction medium consisting of DMEM/F-12 medium, 15% FBS (10099-141, Gibco), 1% penicillin, 1% streptomycin, 0.5 mM IBMX, 1 μM dexamethasone, 1 μg/mL insulin, 1 μM rosiglitazone and 1 nM 3,3′,5-triiodo-*l*-thyronine (T3) and cultured at 37°C in a 5% CO_2 incubator. After 48 h, the induction medium was replaced with maintenance medium containing 1 μg/mL insulin and 1 nM T3 and the cells were then cultured in maintenance medium for an additional 7 days.

C3H/10T1/2 cell culture and osteogenic induction

C3H/10T1/2 mesenchymal stem cells (ATCC, Cat#CCL-226; American Type Culture Collection, Manassas, VA, USA) were cultured in MEM (11095-080, Gibco, Grand Island, NY, USA) supplemented with 1% glutamax (GNM-21051, GENOM2002, Hangzhou, China), 1% sodium pyruvate (GNM-11444, GENOM2002) non-essential amino acids (11140-050, Gibco) and 10% FBS (10099-141, Gibco) at 37°C with 5% CO_2. For osteogenic induction, C3H/10T1/2 cells were induced with 10% FBS in osteogenic medium (MEM supplemented with 50 μmol/L ascorbic acid, 0.1 μmol/L dexamethasone, and 10 mmol/L β-glycerol phosphate). For ALP staining, the cells were maintained in differentiation medium for 8 days. For alizarin red (ARS) staining, the cells were maintained in differentiation medium for 21 days.

C2C12 cell culture and induction

For BAD differentiation, C2C12 cells were cultured in medium containing 10% FBS, 10 μM bexarotene, 0.5 mM isobutylmethylxanthine, 125 μM indomethacin, 5 μm dexamethasone, 850 nM insulin and 1 nM T3 for 48 h. Cells were then grown in medium containing 10% FBS, 850 nM insulin and 1 nM T3 for another 3 days. To stimulate thermogenic gene expression, cells were incubated with 10 μM forskolin (fsk) for 4 h.[42] BAD differentiation of these cells was then evaluated by oil red O staining, and by analysis of BAD markers Ucp-1 and PGC-1-α via western blotting. For osteoblastic differentiation, C2C12 cells were treated with medium containing 10% FBS, 0.2 mM ascorbic acid, 10 nmol/L dexamethasone, and 1 μmol/L β-glycerol phosphate, 5 μg/mL insulin, 0.5 mM isobutylmethylxanthine and 10 nM all-trans retinoic acid for 7 days for ALP staining or 14 days for ARS staining.

Cell treatment with S100A8/A9 recombinant protein (RP), rapamycin, and NF-κB inhibitor

BMSC and C3H/10T1/2 were treated with 200, 500, and 1000 ng/mL of endotoxin-free S100A8/A9 RP (8916-S8-050, R&D, USA) for 7 days in osteogenic medium. C2C12 stromal cells were treated with 100, 200, and 300 ng/mL of S100A8/A9 RP for 5 days in osteogenic medium. BPADs and BADs induced from C2C12 cells (C2C12 BADs) were treated with rapamycin (HY-10219, MCE, shanghai, China) ranging from 4 to 12 nM for 12h before cells and CM were collected. For NF-κB inhibition, C2C12 BADs were treated with 10 μM SN50 (HY-P0151, MCE) and 10 nM QNZ (EVP4593, Selleck, shanghai, China) for 2 h and 24 h, respectively. For TLR4 inhibition, C3H/10T1/2 were treated with S100A8/A9 RP and 200 nM TAK-242(A3850, Apexbio, USA) for 7 days in osteogenic medium.

Cell viability assay

WST-8 assay was performed using Cell Counting Kit-8 (CCK-8, CK04-500T, Dojindo, Japan) colorimetric assay to assess cell proliferation following the manufacturer's protocol. C2C12, C3H/10T1/2 cells and BMSCs were seeded into 96-well plates at a density of 5×10^4 cells per well. The CCK-8 reagent was added to these cells and incubated at 37°C for 0.5 h after S100A8/A9 treatment. The absorbance (optical density) at 450 nm was measured to analyze cell viability.

mRNA array

Total RNA was extracted from primary BMSCs or BAT of the control or $Rheb^{AD}$ KO mice using TRIzol reagent (Invitrogen, Carlsbad, CA, USA) according to the manufacturer's instructions. For mRNA array assays, samples were submitted to Shanghai Biotechnology Corporation for hybridization on an 8 × 60 K Agilent SurePrint G3 Mouse Gene Expression Microarray (V2) (Agilent Technologies, Santa Clara, CA, USA). Each microarray chip was hybridized to a single sample labeled with Cy3. Background subtraction and normalization were performed. Finally, mRNAs with expression levels differing by at least 3-fold between the control and $Rheb^{AD}$ KO mice were selected ($p < 0.05$, Student's t-test).

RNA sequencing

Total RNA was extracted from control or $Rheb^{BAD}$ KO mice using TRIzol reagent (Invitrogen) following the manufacturer's protocol. Total RNA quantity and purity were analyzed using a Bioanalyzer 2100 and an RNA 6000 Nano LabChip kit (Agilent), with RNA integrity values of >7.0. Poly(A) RNA was purified from total RNA (5 μg) using poly-T oligo-attached magnetic beads in two rounds of purification. Following purification, the mRNA was fragmented into small pieces using divalent cations under elevated temperature. Then the cleaved RNA fragments were reverse-transcribed to create the final cDNA library in accordance with the protocol for the TruSeq RNA Sample Preparation v.2 (cat. no. RS-122-2001, RS-122-2002) (Illumina Inc., San Diego, CA, USA); the average insert size for the paired-end libraries was 300 bp (±50 bp). The paired-end sequencing was carried out on an Illumina Hiseq 2500 following the manufacturer's recommended protocol. Before assembly, low-quality reads were removed using Trimmomatic software (www.usadellab.org) and 6G clean reads were obtained. Sequencing reads were aligned to the reference genome (mm10) using the HISAT2 package. The mapped reads of each sample were assembled and counted using the featureCounts package. After a matrix of read counts was generated, differential gene expression was analyzed using the R package edgeR and statistical significance was assessed by exact binomial test. Differentially-expressed genes were selected by the R package with log2 (fold change) values of ≥ 1 or log2(fold change) values of ≤ -1 and with statistical significance of $p < 0.05$.

Lentivirus infection

BPADs were infected with lentivirus carrying the control (Genechem Co., Ltd, Shanghai, China), Rheb shRNA (contract number: GIDL0229913, Genechem), or S100A8 siRNA (contract number: GIDL0295847, Genechem) according to the manufacturer's protocol. The sequence of Rheb-shRNA was GCCAATTTGTTGATTCCTA. The sequence of S100A8-siRNA was CAACCTCATTGATGTCTACCA.

Cre-expressing adenovirus infection

Bone marrow derived macrophages (BMDMs) of $Rheb^{FL/FL}$ mice were infected with adenovirus encoding Cre recombinase (Ad-Cre, GCD0299190, Genechem), according to the manufacture's protocol. BMDMs of $Rheb^{FL/FL}$ mice infected with the control virus (vectors not encoding Ad-Cre) were used as a control (Ad-NC).

Real time RT-PCR analysis

Mice were euthanized, and total RNA in BAT was rapidly extracted using RNAiso Plus (9109, TaKaRa, Beijing, China) and reverse-transcribed into cDNA using the PrimeScript RT reagent kit (RR047A, TaKaRa). Real-time quantitative PCR (RR420A, TaKaRa) analysis was performed with specific gene primers (Table S1) using an ABI 9700 Thermal Cycler (Applied Biosystems, Foster City, CA, USA). Quantification of RNA expression levels was performed using the $2^{-\Delta\Delta CT}$ method, and β-actin was used as a positive control.

Western blotting, silver staining, and immunohistochemical assay

For total protein extraction, cells were lysed in RIPA buffer containing 50 mM Tris-HCl pH 8, 150 mM NaCl, 1% Triton X-100, 0.1% sodium deoxycholate, 0.1% SDS, and 1× protease inhibitor cocktail (Roche, Basel, Switzerland). Lysates were boiled in 2× SDS sample buffer. Proteins were separated by SDS-PAGE, followed by transferring to nitrocellulose membranes (Bio-Rad, Hercules, CA, USA) for immunoblotting with relevant antibodies, or silver staining using the Fast Silver Stain kit (P00175, Beyotime) according to the manufacturer's instructions. For bone histology and histomorphometric analysis, femora and tibiae were decalcified for 20–30 days in decalcification solution (1.45% ETDA, 1.25% NaOH, 1.5% glycerol, pH 7.3) at 4°C. Decalcified bones were processed and embedded in paraffin, and 5 μm sagittal-oriented sections were prepared for histological analyses. For morphological analysis, sections were stained with a modified hematoxylin and eosin (H&E) stain, and osteoclasts were stained using an acid phosphatase, leukocyte (TRAP) kit (Sigma, #387a), which is quantified using Oc.S/BS (osteoclasts surface to bone surface) parameter by OSTEOMEASURE system. Immunohistochemical staining was performed using primary antibodies listed in the key resources table which were added and incubated at 4°C overnight. Images were screened using an Axio Scope A1 microscope (Carl Zeiss Microscopy GmbH, Jena, Germany) and processed using Osteomeasure System (OsteoMetrics, Decatur, GA, USA). Osteoblasts surface to bone surface (Ob.S/BS), osteoclasts surface to bone surface (Oc.S/BS), OSX positive cell number over bone perimeter

(N.OSX/B.Pm) and OCN positive cell number over bone perimeter (N·OCN/B.Pm) in 5 randomly selected visual fields per specimen were measured and quantitated by OSTEOMEASURE system.

Secreted protein analysis by western blotting

500 μL of culture medium were added to an Amicon Ultra-0.5 device (UFC50030, Merck-Millipore, Darmstadt, Germany) and centrifuged for 30 min at 12,000 × *g* according to the user manual. An equal volume of 2× Laemmli buffer (125 mM Tris-HCl, pH 6.8, 4% sodium dodecyl sulfate, 20% glycerol, 100 mM dithiothreitol, 0.02% bromophenol blue) was mixed with the ultrafiltrate and boiled at 100°C for 10 min.

Immunofluorescence

Femora, tibiae, and BAT dissected from the mice were fixed using 4% paraformaldehyde in phosphate-buffered saline (PBS) at 4°C for 24 h. Brain dissected from the mice which were transcardially perfused with saline followed by 4% paraformaldehyde (PFA) were post-fixed in 4% PFA at 4°C for 24 h. Femora and tibiae decalcified in 15% EDTA (pH 7.4) at 4°C for 14 days. The tissues were embedded in paraffin, and 5-μm sagittal-oriented of femora, tibiae, and BAT, or coronal-oriented of brain sections were prepared for histological analyses. The sections were incubated with primary antibodies against perilipin 1 (PLIN1, #9349,1:150,CST), P-P65-S276 (AP0123, 1:100, ABclonal, Woburn, MA, USA), Rheb (15924-1-AP, 1:100, Proteintech), or Myd88 (A0980, 1:50, ABclonal) and labeled with secondary antibodies for 1 h in the dark. After labeling, cells were incubated with DAPI for 5 min. Images were acquired with an Olympus 200 M microscope (Olympus, Tokyo, Japan). The numbers of positively-stained cells in the whole medullary space or bone trabecula per femur or tibia in three sequential sections per mouse in each group were counted using Image Pro Plus software.

Micro-computed tomography (μCT) analyses

Distal femora and proximal tibiae were fixed overnight in 4% paraformaldehyde and then analyzed by high-resolution μCT (Scanco Medical μCT100, Brüttisellen, Zurich, Switzerland), with a voltage of 55 kVp, an intensity of 200 μA, a resolution of 5 μm per pixel and an exposure of 230 ms. The trabecular bone and cortical bone, which is proximal to the distal growth plate for the femora and distal to the proximal growth plate for the tibiae, was analyzed starting at the inferior border of the growth plate and extended a further longitudinal distance of 200 slices (1mm). The three-dimensional structure and morphometry were reconstructed by three-dimensional model visualization software (μCT Ray V4.2) and data analyzed by data analysis software (μCT Evaluation Program V6.6) for trabecular bone volume fraction (BV/TV), trabecular thickness (Tb. Th), trabecular number (Tb. N), trabecular separation (Tb. Sp), the cortical thickness (Ct. Th) and cortical BV/TV.

Frozen sections and ALP staining

Mice were euthanized and the femora were removed and fixed with ALP solution (8% paraformaldehyde, L-Lysine (Sigma-Aldrich) and sodium periodate (Merck, Palo Alto, CA, USA). After 24 h, femora and tibiae were decalcified for 20–30 days in decalcification solution at 4°C. The tissues were then transferred into 30% sucrose for 24 h to dehydrate, and then 5 μm sagittal-oriented sections were prepared using a Leica CM1850 frozen microtome (Leica, Wetzlar, Germany). For ALP staining, the tissues were incubated at 65°C for 1 h to remove the OCT embedding agent, then stained using an ALP staining kit (Beyotime Institute of Biotechnology) and quantified using Ob.S/BS (Osteoblasts surface to bone surface) parameter by OSTEOMEASURE system.

Hard tissue sections

Mice were euthanized and then the femora were removed and fixed with 4% paraformaldehyde for 24 h. 3-month-old mice were injected with calcein (c0875, Sigma-Aldrich) (15 mg/kg, i.p.) 10 and 3 days before euthanasia. Tissues were then gradually dehydrated by 70–100% alcohol, and finally placed in xylene for 2 days. After embedding using a plastic embedding agent, the tissues were cut with a hard tissue microtome (EXAKT Advanced Technologies GmbH, Norderstedt, Germany). For calcium salt detection, tissues were stained with a Von Kossa staining kit (ab150687, Abcam, UK) according to the manufacturer's protocol. Image acquisitions were performed using Zeiss microscope and quantified using Image pro plus. For calcein detection, tissues were directly screened using a confocal laser scanning microscope (Olympus FV1000, Tokyo, Japan) and quantified by OSTEOMEASURE system.

Blood biochemical studies

An automatic chemical chemistry analyzer (Catalyst Dx, IDEXX, USA) was used to measure concentrations of circulating triglycerides (98-11086-01, Catalyst, USA). Circulating glycerol (XFP17067, GEMIC, Nanjing, China) and circulating free fatty acids (#BC0595, Solarbio, Beijing, China) were determined according to the manufacturer's instructions.

Enzyme-linked immunosorbent assay (ELISA)

Blood samples were collected from 8-week-old mice by 1.5 mL centrifuge tubes at room temperature and allowed to stand still for 1h. Serum were collected from the upper layer after clotting and centrifuged at 3000 rpm for 10 min at room temperature. The protein levels of S100A8, S100A9, PINP, CTX-I, leptin and noradrenaline in the serum were measured using a mouse S100A8 ELISA kit (E-EL-M1343c, Elabscience, Wuhan, China), a mouse S100A9 ELISA kit (E-EL-M3049, Elabscience),a mouse PINP ELISA kit (E-EL-M0233c, Elabscience), a mouse CTX-I ELISA

kit (CEA665Mu, cloud-clone, Wuhan, China), a mouse leptin ELISA kit (E-EL-M3008, Elabscience) and a mouse noradrenaline ELISA kit (CSB-E07870m, CUSABIO, Wuhan, China) according to the manufacturer's instructions.

S100A8/A9 neutralization *in vitro* and *in vivo*

BMSCs from wild-type C57BL/6J mice were treated with conditioned medium (CM) from primary BADs of *Rheb*^{AD} KO and *Rheb*^{BAD} KO mice, in the presence or absence of 500 ng/mL S100A8/A9 neutralizing antibody (NA) for 36 h before complete confluence. For intramedullary injection, 0.3 × 13RWLB needles (KDL-94, KDL, shanghai, China) were used to perforate the joint cavity and the tibia marrow cavity. Then, 2.5 μg (4μL) S100A8/A9 neutralizing antibody (697504, Biolegend, San Diego, CA, USA) was injected into the right tibial marrow cavity of 5-month-old and 10-month-old male *Rheb*^{BAD} KO mice, using Hamilton needles (763301, Hamilton, New York, NY, USA) twice a week, while 2.5 μg IgG antibody (409306, Biolegend) as a control was injected into the left tibia. Mice were euthanized after 2 months of treatment, and tibiae were collected for bone metabolism experiments. For tail vein injection, 60ul (200μg/kg) S100A8/A9 neutralizing antibody (697504, Biolegend, San Diego, CA, USA) was injected into the tail vein of 10-month-old *Rheb*^{BAD} KO mice using 1mL syringe, while 60ul (200μg/kg) IgG antibody (409306, Biolegend) as a control was injected into the tail vein of littermate 10-month-old *Rheb*^{BAD} KO mice twice a week. Mice were euthanized after 3 months of treatment, and femurs were collected for bone metabolism experiments.

Glucose tolerance test (GTT) and insulin tolerance test (ITT)

For glucose tolerance tests (GTTs), mice were fasted overnight (16 h) and treated with an intraperitoneal injection of glucose (1 g/kg). For insulin tolerance tests (ITTs), mice were intraperitoneally treated with insulin (0.75U/kg) after 3 h fasting. Tail venous blood was collected at 0, 15, 30, 45, 60, 90, and 120 min after glucose or collected at 0, 15, 30, 45, 60, and 90 min after insulin injection, and blood glucose levels were measured using the glucometer.

Cold and thermal neutrality exposure studies

For cold and thermal neutrality exposure experiments, mice were placed in the temperature controlled incubators (Caron Products & Services Inc) at 4°C or 30°C for 7 days on a 12hrs light/dark cycle with free access to water and food. Control mice were kept at room temperature (22°C). At the end of the experiment, mice were euthanized and BAT were isolated to extract RNA and protein.

Metabolic phenotyping

Indirect calorimetry experiments were conducted with a Comprehensive Lab Animal Monitoring System (CLAMS, Columbus Instruments, USA). Mice in the CLAMS were fed *ad libitum*. Results of oxygen consumption, respiratory exchange ratio, energy expenditure, and food intake were collected and analyzed.

Bioinformatics analysis

The transcriptomes of BMSCs and BAT were subjected to gene ontology (GO) and KEGG pathway analysis using the ClusterProfiler and enrichplot Bioconductor R packages, following website guidelines. The cnetplot function was used to visualize GO functional enrichment results. Ggplot2 was used to generate a volcano plot.

QUANTIFICATION AND STATISTICAL ANALYSIS

Statistical analyses were conducted using GraphPad Prism 9.5 software (GraphPad Prism, San Diego, CA, USA). Data are shown as box-and-whisker plots (with median and interquartile ranges) from max to min, with all data points shown of at least three independent experiments. After testing for normality by Kolmogorov-Smirnov test, statistical significance between groups were analyzed. Except data in Figure S2 (glycerol) are non-normally distributed, other data are normally distributed. Otherwise, for analyzing statistical significance between 2 groups, two-tailed unpaired *t*-tests were used. For more than 2 groups, one-way analysis of variance with multiple comparisons were used, followed by the Bonferroni *post-hoc* test for significance. A p-value of <0.05 was considered statistically significant. Photomicrographs and Western blot images are representative of at least three independent experiments.